

CHARACTERIZATION AND FATIGUE BEHAVIOR OF Ti-6Al-4V FOAMS

A THESIS SUBMITTED TO  
THE GRADUATE SCHOOL OF NATURAL AND APPLIED SCIENCES  
OF  
MIDDLE EAST TECHNICAL UNIVERSITY

BY

EMİN ERKAN AŞIK

IN PARTIAL FULFILLMENT OF THE REQUIREMENTS  
FOR  
THE DEGREE OF MASTER OF SCIENCE  
IN  
METALLURGICAL AND MATERIALS ENGINEERING

AUGUST 2012

Approval of the thesis:

**CHARACTERIZATION AND FATIGUE BEHAVIOR OF Ti-6Al-4V  
FOAMS**

submitted by **EMİN ERKAN AŞIK** in partial fulfillment of the requirements for the degree of **Master of Science in Metallurgical and Materials Engineering Department, Middle East Technical University** by,

Prof. Dr. Canan ÖZGEN  
Dean, Graduate School of **Natural and Applied Sciences**

\_\_\_\_\_

Prof. Dr. C. Hakan GÜR  
Head of Department, **Metallurgical and Materials Engineering**

\_\_\_\_\_

Prof. Dr. Şakir BOR  
Supervisor, **Metallurgical and Materials Engineering, METU**

\_\_\_\_\_

**Examining Committee Members:**

Prof. Dr. Kadri AYDINOL  
Department of Metallurgical and Materials Eng., METU

\_\_\_\_\_

Prof. Dr. Şakir BOR  
Department of Metallurgical and Materials Eng., METU

\_\_\_\_\_

Assoc. Prof. Dr. Nuri DURLU  
Department of Mechanical Eng., TOBB-ETU

\_\_\_\_\_

Assoc. Prof. Dr. Arcan Fehmi DERİCİOĞLU  
Department of Metallurgical and Materials Eng., METU

\_\_\_\_\_

Assist. Prof. Dr. Ziya ESEN  
Department of Materials Science and Eng., Çankaya University

\_\_\_\_\_

**Date:** 08.08.2012

**I hereby declare that all information in this document has been obtained and presented in accordance with academic rules and ethical conduct. I also declare that, as required by these rules and conduct, I have fully cited and referenced all material and results that are not original to this work.**

Name, Last name : Emin Erkan Aşık

Signature :

# **ABSTRACT**

## **CHARACTERIZATION AND FATIGUE BEHAVIOR OF Ti-6Al-4V FOAMS**

Aşık, Emin Erkan

M.Sc., Department of Metallurgical and Materials Engineering

Supervisor: Prof. Dr. Şakir Bor

August 2012, 65 pages

Porous Ti-6Al-4V alloys are widely used in the biomedical applications for hard tissue implantation due to its biocompatibility and elastic modulus being close to that of bone. In this study, porous Ti-6Al-4V alloys were produced with a powder metallurgical process, space holder technique, where magnesium powders were utilized in order to generate porosities in the range of 50 to 70 vol. %.

In the productions of Ti-6Al-4V foams, first, the spherical Ti-6Al-4V powders with an average size of 55  $\mu\text{m}$  were mixed with spherical magnesium powders sieved to an average size of 375  $\mu\text{m}$ , and then the mixtures were compacted with a hydraulic press under 500 MPa pressure by using a double-ended steel die and finally, the green compacts were sintered at 1200°C for 2 hours under high purity argon gas atmosphere.

Scanning electron microscope investigation of produced foams has shown that the foams consist of spherical, interconnected macropores and irregular shaped micropores.

Monotonic compression tests conducted on processed foams under quasi-static test conditions exhibited yield strengths varying between 69 to 167 MPa and elastic moduli between 4 to 12 GPa.

Processed foams were also dynamically tested under compression - compression fatigue with a stress ratio of 0.1. Foams with different pore contents exhibited similar fatigue response when maximum applied stress was normalized with respect to the average yield strength of the corresponding foam. It was found that foams were fatigue immune with a practical limit of  $10^6$  cycles under a maximum applied stress of  $0.75 * (\sigma_{\max} / \sigma_{\text{yield}})$ .

**Keywords:** Powder Metallurgy, Porosity, Foam, Ti-6Al-4V, Magnesium, Space holder, Compression, Fatigue

# ÖZ

## GÖZENEKLİ Ti-6Al-4V ALAŞIMLARININ KARAKTERİZASYONU VE YORULMA DAVRANIŞLARI

Aşık, Emin Erkan

Yüksek Lisans, Metalurji ve Malzeme Mühendisliği Bölümü

Tez Yöneticisi: Prof. Dr. Şakir Bor

Ağustos 2012, 65 sayfa

Kemiğe benzer elastik modüle sahip, biyouyumlu gözenekli Ti-6Al-4V alaşımları biyomedikal uygulamalarda sert doku implantlı olarak yaygınlıkla kullanılmaktadır. Bu çalışmada, magnezyum tozlarının boşluk yapıcı olarak kullanıldığı bir toz metalurjisi yöntemi ile hacimce % 50 ile 70 arasında gözenek içeren Ti-6Al-4V alaşımları üretilmiştir.

Gözenekli Ti-6Al-4V alaşımlarının üretiminde ilk olarak ortalama 55 µm çapındaki küresel Ti-6Al-4V tozları, ortalama 375 µm'ye elenmiş küresel magnezyum tozlarıyla karıştırılmış daha sonra 500 MPa basınçla hidrolik press kullanılarak çift uçlu çelik kalıpta sıkıştırılmış ve sonrasında 1200°C sıcaklıkta 2 saat süre ile yüksek saflıkta argon gazı altında sinterlenmiştir.

Üretilen gözenekli Ti-6Al-4V alaşımları taramalı electron mikroskobu ile incelenmesi sonucunda ve bütün köpüklerde küresel birbiri ile bağlantı makro gözenekler ve düzensiz şekilli mikro gözenekler bulunduğu saptanmıştır.

Üretilen Ti-6Al-4V köpüklere sabit hızda, yarı durağan basma testleri sonucunda köpüklerin akma dirençlerinin 69 ile 167 MPa, elastic modüllerinin ise 4 ile 12 GPa arasında değiştiği gözlenmiştir.

Ayrıca, üretilmiş olan köpükler 0.1 gerilme oranında basma - basma yorulma testleri ile dinamik olarak test edilmiştir. Uygulanan maksimum gerilim ilgili köpüğün ortalama akma dayancı ile normalize edildiğinde farklı oranlarda boşluk içeren köpüklerin benzer davranış sergilediği görülmüştür. Üretilen köpüklerin,  $10^6$  döngü pratik limit olarak kabul edildiğinde,  $0,7*(\sigma_{max}/\sigma_{akma})$  oranında gerilim altında yorulmaya dirençli olduğu bulunmuştur.

**Anahtar Kelimeler:** Toz Metalurjisi, Gözenek, Ti-6Al-4V, Magnezyum, Boşluk Yapıcı, Basma, Yorulma

**To My Family,**

## ACKNOWLEDGMENTS

I would like to express my deepest appreciation to Prof. Dr. Şakir Bor for his supervision, guidance, support and patience throughout the study.

I am grateful to Prof Dr. Rıza Gürbüz, Assoc. Prof. Dr. Arcan DERİCİOĞLU, and Assist. Prof. Dr. Eren Kalay for their helps and supports during the study.

I would like to express my sincere appreciation to Assist Prof Dr. Ziya ESEN and İpek NAKAŞ for their wise advices and comments on the study.

I would like to thank all the staff of the Department of Metallurgical and Materials Engineering and Central Laboratory for their effort and help in testing and characterization.

I would specially thank to my lab mates İpek NAKAŞ, Bensu TUNCA, Zeynep BÖLÜKOĞLU, and Ezgi BÜTEV.

I owe great debt to Sıla AKMAN, Deniz BİLGİN, Burak AKTEKİN, and many other friends who endlessly supported me and endured my sullen face.

This thesis has been financially supported by M.E.T.U. Research Fund and TÜBİTAK through the projects BAP-03-08-2011-008 and 108M118, respectively.

# TABLE OF CONTENTS

ABSTRACT .....	iv
ÖZ .....	vi
ACKNOWLEDGMENTS .....	ix
TABLE OF CONTENTS .....	x
LIST OF TABLES .....	xii
LIST OF FIGURES .....	xiii
CHAPTERS .....	1
1.INTRODUCTION .....	1
2.THEORETICAL BACKGROUND .....	3
2.1 Titanium and Titanium Alloys .....	3
2.1.1 Titanium and Its Alloys as a Biomaterial.....	4
2.2 Solid Metal Foams .....	6
2.2.1 Production of Porous Titanium and Titanium Alloys.....	8
2.2.1.1 Loose Powder Sintering .....	10
2.2.1.2 Space Holder Technique .....	11
2.3 Conventional Sintering .....	12
2.4 Mechanical Behavior of Porous Materials.....	14
2.4.1 Compressive Response .....	14
2.4.2 Fatigue Response .....	17
3.EXPERIMENTAL PROCEDURE .....	22
3.1 Powders Used.....	22
3.2 Production of Porous Ti-6Al-4V Alloys.....	25

3.3 Characterization Studies .....	28
3.3.1 Particle Size Distribution .....	28
3.3.2 Density and Porosity Measurements.....	29
3.3.3 X-ray Diffraction Analysis.....	30
3.3.4 Scanning Electron Microscopy Studies .....	30
3.3.5 Mechanical Characterization.....	31
3.3.5.1 Monotonic Compression Tests.....	31
3.3.5.2 Fatigue Tests .....	32
4.RESULTS AND DISCUSSION .....	34
4.1 Porosity and Pore Characteristics .....	34
4.2 X-ray Analysis and Microstructure.....	38
4.3 Mechanical Behavior of Ti-6Al-4V Foams .....	43
4.3.1 Compressive Behavior .....	43
4.3.1.1 Stress Strain Curves .....	43
4.3.1.2 Cyclic Compressive Behavior.....	46
4.3.1.3 Compressive Behavior - Porosity Relations .....	48
4.3.1.4 Fracture Surfaces after Compression Tests.....	49
4.3.2 Fatigue Behavior .....	51
4.3.2.1 Contraction - # of Cycles Curves.....	51
4.3.2.2 S-N Curves.....	54
4.3.2.3 Fracture Surfaces of Fatigue Tested Foams.....	56
5.CONCLUSION.....	60
REFERENCES.....	62

## LIST OF TABLES

### TABLES

Table 2.1 Mechanical Properties of Ti-6Al-4V Alloy [2,5] .....	4
Table 2.2 Some applications of synthetic materials, adapted from Biomaterials Science: An Introduction to Materials in Medicine [6] .....	5
Table 4.1 Porosity characteristics of the foams .....	34
Table 4.2 Weight percentages of the present phases .....	41
Table 4.3 Mechanical Properties of the Foams .....	46

## LIST OF FIGURES

### FIGURES

Figure 2.1	Metallic foams (a) two dimensional honeycomb, (b) three dimensional foams with open cells, (c) three dimensional foams with closed cells [17].....	6
Figure 2.2	Summary of the production methods of metal foams [18].....	7
Figure 2.3	Georgian Tech production route for hollow spheres [21] .....	9
Figure 2.4	Schematic presentation of loose powder method [19].....	10
Figure 2.5	General steps of processing foams with space holder technique adapted from Banhart et al. [18].....	11
Figure 2.6	Flow mechanisms occurring during sintering [29].....	14
Figure 2.7	A typical compressive stress - strain curve of foams showing general characteristic regions .....	15
Figure 2.8	Elastic bending and buckling of the cell walls of an open pore, a) initial state b) elastically deformed stage [17] and F showing the loading direction and points .....	16
Figure 2.9	A schematic representation on the formation of intrusions and extrusions. The arrows show direction of the loading [35].....	18
Figure 2.10	Definitions of the stress terms [35].....	19
Figure 2.11	Change of strain with respect to number of cycles in compression compression fatigue [37] .....	19
Figure 2.12	Typical behaviors of foams under compression compression loading. (a) Failure occurs with broadening of a single crash band, (b) Failure occurs with broadening of multiple crush bands [38] .....	20

Figure 3.1 Particle size distribution of (a) Ti-6Al-4V, (b) Mg powders. Solid lines represent volume percentages and dashed lines show cumulative frequency percentages.....	23
Figure 3.2 SEM micrographs of (a) Ti-6Al-4V, (b) Mg powders .....	24
Figure 3.3 X-ray diffractogram of the as received Ti-6Al-4V powders .....	25
Figure 3.4 Cold pressed Ti-6Al-4V and Mg mixture compacts. The white and.....	26
Figure 3.5 Cross section of the crucible.....	27
Figure 3.6 Representative steps of foam processing with Mg space holder method .....	28
Figure 3.7 Representative stress-strain curve of foams .....	32
Figure 3.8 Representative contraction- number of cycles.....	33
Figure 4.1 Change of porosity with Mg addition.....	35
Figure 4.2 SEM micrographs showing (a) macropores, .....	37
Figure 4.3 X-ray diffraction Analysis of produced foams .....	39
Figure 4.4 SEM micrographs of the microstructures present in the produced foams (a) 1000x, (b) 10000x .....	40
Figure 4.5 EDX results of the phases (a) $\alpha$ phase, (b) $\beta$ phase .....	42
Figure 4.6 Compressive stress strain curves of highly porous Ti-6Al-4V alloy sintered at 1200°C for 2h under high purity argon gas atmosphere .....	43
Figure 4.7 Collapsed cell walls during compression. Circles showing some of the failed cell walls and white arrow shows the direction of compression .....	44
Figure 4.8 Foams after compression tests (a) 50, 60 (b) 70 Vol. % Mg added foams .....	45
Figure 4.9 Cyclic compression tests showing the residual strain below $\sigma_{yield}$ .....	46
Figure 4.10 Change of Relative elastic modulus of the foam.....	47
Figure 4.11 Mechanical properties of the foams with respect to relative density ...	48

Figure 4.12 SEM micrographs of tested foams (a) general view of fractured surfaces, (b) sinter necks containing tear ridge like appearance, (c) transcrystalline fracture feature with dimples on $\alpha$ laths, (d) dimples .	49
Figure 4.13 Foams failed under cyclic loading. Samples (a) failed with wavy increase in contraction, (b) failed with rapid and sudden increase in contraction .....	52
Figure 4.14 Contraction - # of cycles curves of the processed foams (a) representative curve for foams exhibiting densification, (b) representative curve of the foams not exhibiting densification under quasi-static compression test .....	53
Figure 4.15 S-N curves of the processed foams.....	54
Figure 4.16 Normalized S-N curve of processed foams .....	55
Figure 4.17 Example of a crack growth and fracture.....	56
Figure 4.18 Micrographs showing fatigue crack growth (a) striations, .....	57
Figure 4.19 Micrographs showing fast fracture surfaces (a) dimples, (b) tear ridges, (c) combination of tear ridges and dimples on possible $\alpha$ laths.....	58

# CHAPTER 1

## INTRODUCTION

Titanium and titanium alloys have been used in engineering for structural and functional applications such as in aerospace and automotive industries, and biomedical field due to their unique combination of properties such as low density, versatile mechanical properties, high specific strength, high corrosion resistance, good fatigue response, and biocompatibility.

Wood, bone, cork, honeycombs are some of the examples from nature which inspired engineers for the production of solid foams. A material's properties can be altered and modified to have distinct thermal, vibrational or mechanical characteristics by introducing pores into the structure.

In the recent years, titanium and its alloys are extensively used in porous form as biomedical materials for hard tissue replacements such as dental implants hip and knee joints etc. Porous titanium and titanium alloys have elastic modulus value close to that of human bones with enough strength. This reduces the stress shielding effect which is weakening of the bone due to presence of stiffer implant material. In addition, porous structure allows bone tissue ingrowth through the porous metal, establishing better mechanical adhesion.

Porous metals can be produced by mainly two routes: liquid and solid state processes. Liquid state processed are preferred for metals which have low melting points, such as aluminum, and low reactivity. On the other hand, solid state

operations or sintering processes are used for metals with high melting points and high reactivity. Production of porous titanium and its alloys involves a sintering process.

Porous titanium and titanium alloys are processed mainly by five different powder metallurgical methods; loose powder sintering, space holder method, sintering of hollow spheres, gas entrapment method and replication method.

Foams produced with different methods have different pore characteristics such as pore type, interconnection, size, shape, distribution and volume fraction. Space holder method is a simple and practical method which enables easy control of pore characteristics by controlling the fraction, size and geometry of spacer powders. Magnesium, NaCl, carbamide, starch are some examples of frequently used spacers for the production of porous titanium and titanium alloys. Among the listed spacers, magnesium is an attractive space holder due to its dual function. Magnesium spacers melt and evaporate during the sintering operation and create pores as well as a protective atmosphere due to higher reactivity with oxygen.

Mechanical properties of the processed foams are also important. As mentioned above the foams should have enough strength with low modulus to be used in bone replacement. In addition compressive- compressive fatigue response of the porous metals is crucial since when used as hard tissue implants they will mostly exposed to cyclic compressive loading.

To conclude, in the present study Ti-6Al-4V alloy foams has been processed with 50 to 70 vol. % magnesium spacer addition. Magnesium spacers have been spherical in shape in order to reduce stress concentrations and in the size range of 250 – 600  $\mu\text{m}$  for optimum bone ingrowth capability. Density and pore characteristics of the produced foams will be investigated. In addition compressive mechanical properties as well as fatigue response of the foams will be determined in order to investigate the applicability of the foams as an implant material.

## CHAPTER 2

### THEORETICAL BACKGROUND

#### 2.1 Titanium and Titanium Alloys

Titanium (Ti) and its alloys are used in engineering applications due to their unique combination of properties such as low density, high melting point, high corrosion resistance, perfect mechanical properties and good biocompatibility. Ti and its alloys are used for structural and functional applications in aerospace, automotive, chemical and biomedical industries [1].

Titanium exhibits an allotropic phase transformation at 882°C from lower temperature stable  $\alpha$  phase to high temperature stable  $\beta$  phase. The crystal structure of  $\alpha$  phase is hexagonal closed packed (HCP), whereas  $\beta$  phase is body centered cubic (BCC). The alloying elements added to Ti are named as  $\alpha$  and  $\beta$  stabilizers according to the change they do on the transition temperature. Aluminum, oxygen, nitrogen and carbon are some of the  $\alpha$  stabilizing elements whereas vanadium, chromium, manganese, iron, cobalt and nickel are some  $\beta$  stabilizers. Titanium alloys are named in three categories as  $\alpha$  alloys,  $\alpha+\beta$  alloys and  $\beta$  alloys according to the stable phases at room temperature [2].

The mechanical properties of Ti show a distinct anisotropy due to the presence of HCP crystal structure. Elastic modulus of  $\alpha$ -Ti varies between 100 to 145 GPa [2].

Ti-6Al-4V (wt. %) is the mostly used titanium alloy in industry [3]. Ti-6Al-4V is an  $\alpha+\beta$  alloy with a  $\beta$  transus temperature of 995°C. Cooling of the alloy from above the  $\beta$  transus temperature results in a fully lamellar microstructure. The mechanical properties of the fully lamellar alloy are significantly affected from  $\alpha$  colony size which is controlled by the cooling rate [4]. Mechanical properties of the alloy are given in Table 2.1.

**Table 2.1** Mechanical Properties of Ti-6Al-4V Alloy [2,5].

<b>Elastic Modulus (GPa)</b>	<b>Yield Strength (MPa)</b>	<b>Tensile Strength (MPa)</b>	<b>Hardness (HV)</b>	<b>Fatigue Strength (R= -1) (MPa)</b>
110-140	800 - 1100	900 - 1200	300 - 400	500-700

Yield strength, fracture strength and high cycle fatigue life of Ti-6Al-4V alloy increases with smaller  $\alpha$  colony size. Above the cooling rates of 1000°C/min the pre-mentioned parameters shows a drastic increases due to formation of martensitic  $\alpha'$  however ductility of the alloy decreases. This decrease is also related to the change in fracture mode. At low cooling rates a ductile transcrystalline dimple type of fracture is observed whereas at higher cooling rates the fracture appearance changes to a ductile intercrystalline dimple type [2, 4].

### **2.1.1 Titanium and Its Alloys as a Biomaterial**

Metallic biomaterials are used especially in three categories; artificial hip, knee joints, screws and plates for internal fixation of fractured bones and dental implants. Stainless steels, cobalt-chrome based alloys and titanium alloys are used as metallic biomaterials in structural biomedical applications. The most important reason for those materials to be chosen in biomedical applications is biocompatibility. Table 2.2 shows the materials uses in biomedical applications [6]. Biocompatibility can be defined in three ways; the ability of the materials to perform with a response similar to the response of the host, the quality of not having toxic or injurious effects on the biological system and comparison of the tissue response produced through the close

association of the implanted candidate material to its implant site within the host animal to that tissue response recognized and established as suitable with control materials [7].

**Table 2.2** Some applications of synthetic materials, adapted from Biomaterials Science: An Introduction to Materials in Medicine [6].

Application	Types of materials
Joint replacements (hip, knee)	Titanium, Ti–Al–V alloy, stainless steel, polyethylene
Bone plate for fracture fixation	Stainless steel, cobalt–chromium alloy
Dental implant for tooth fixation	Titanium, Ti–Al–V alloy, stainless steel, polyethylene Titanium, alumina, calcium phosphate
Heart valve	Reprocessed tissue, stainless steel, carbon

In order to enhance the biocompatibility, stiffness of the materials used should be close to that of bone in order to reduce or eliminate the effect of stress shielding which is reduction in the mechanical properties of the bone touching to the implanted material [8]. In order to reduce the stiffness of metallic implants porosities are introduced to the structure of the metal. By this way elastic moduli of implants can be reduced to levels below 30 GPa which is the reported range for the elastic moduli of human bones [9]. Other important parameters for an implant are osseointegration and bone ingrowth. Osseointegration was first used for the intimate contact of the Ti implants and the bone surface [10] and bone ingrowth is referred to the ability of the bone to grow through an implant with an outer mesh structure. It was concluded from the investigations of Jasty *et al.* that there was an optimum pore size in the range of 100 – 400  $\mu\text{m}$  size in which bone ingrowth rate was highest [11].

Titanium and titanium alloys satisfy the mentioned conditions for the use in biomedical applications. The presence of passive protective oxide layer provides high corrosion resistance and bio inertness [7]. By this way the implants made from Ti and its alloys do not react in the body. Ti and its alloys can be produced by which a mesh like porous structure can be obtained for bone ingrowth [12]. In the literature Ti and Ti-6Al-4V alloys were produced with porous structures satisfying the mechanical properties close to those of bone [13, 14, 15]. In addition Ti and its alloys exhibits endurance limit under cyclic loading conditions which makes them significant since it annihilates replanting operation and further surgeries.

To conclude, the studies show that long term usage of Ti and titanium alloys as biomedical materials has advantages due to its mechanical and chemical biocompatibility [16].

## 2.2 Solid Metal Foams

A solid foam structure is composed of interconnected network of struts, cell walls from the edge and face of cells. Porous structures are found naturally in wood, cork, honeycombs, bones, etc. Artificial porous structures are used in engineering applications due to their mechanical, thermal, acoustic and vibrational properties. Man made solid foams can be classified in three groups namely; two dimensional honeycomb like structures, three dimensional foams with open cells and three dimensional foams with closed cells (Figure 2.1) [17].

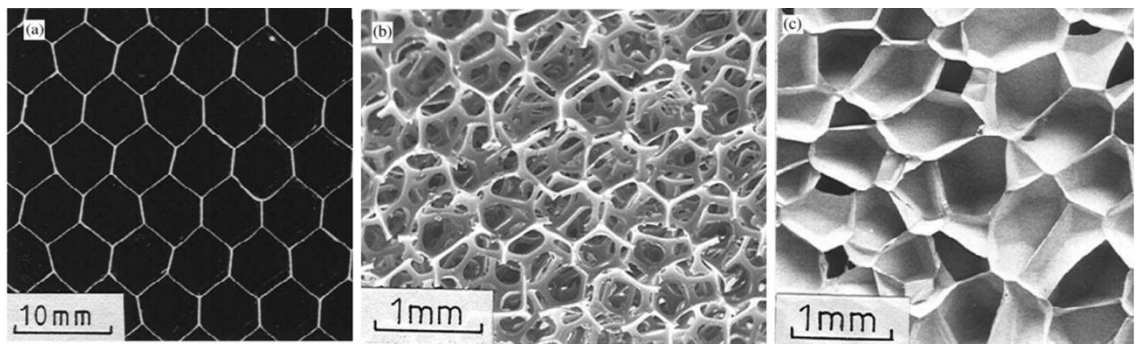


**Figure 2.1** Metallic foams (a) two dimensional honeycomb, (b) three dimensional foams with open cells, (c) three dimensional foams with closed cells [17].

The properties of the foams are dependent up on their pore type, shape, size, amount, uniformity, and interconnection. Different porosity amounts, pore shapes and geometries can be produced with various production methods. With the combination of these characteristics, light weight metals with unique properties such as density, elastic modulus, yield strength, energy absorption capacity, thermal conductivity, air and water permeability, electrical insulation can be produced.

The processing methods of porous metals can be classified into two groups; liquid state processes and solid state processes. Liquid state processes include a melting and casting step. This type of production is suitable for metals with low melting points and reactivity like aluminum; on the other hand, many solid state processes include a sintering step. However, some solid state processes include formation of pores by partial melting of a bulk structure like in the case of space holder technique. Solid state processes are suitable for highly reactive metals with high melting temperatures. Banhart *et al* summarized the production methods and it is shown in Figure 2.2 [18].

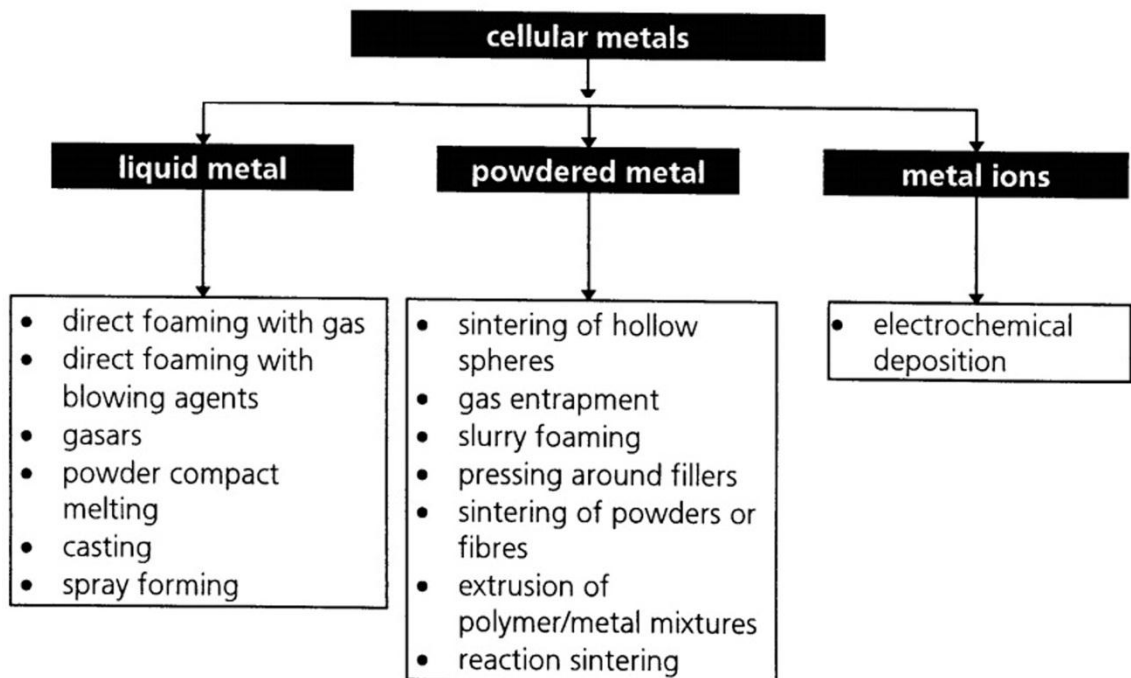


**Figure 2.2** Summary of the production methods of metal foams [18].

### 2.2.1 Production of Porous Titanium and Titanium Alloys

Porous titanium and titanium alloys are mainly produced with powder metallurgy [19]. In this section most frequent production methods will be described in a brief manner. The processes can be grouped into five category; loose powder sintering, space holder method, gas entrapment techniques, hollow sphere sintering, replication method and electro discharge methods [18].

First two methods, loose powder sintering and space holder method, will be described in the following sections.

In the gas entrapment technique, an inert gas is introduced to the system containing metal powders under high pressure and then, densified at elevated temperatures. During densification gas is entrap in the metal matrix. After densification the processed metal is heated up to elevated temperatures, at which the gas expands due to lowering of the mechanical strength of metals at elevated temperatures. This process is hard to operate since it requires high pressures at high temperatures. Oppenheimer *et al.* processed Ti-6Al-4V foams with expansion of argon gas. In their study they compacted Ti-6Al-4V alloy powders and filled the mold with argon gas at a pressure around 0.33 MPa and welded the mould. After that the densification was done in a hot isostatic press at 950°C, 100 MPa pressure. Finally, the expansion of the gas or so called foaming was done at 1030°C at atmospheric pressure. The processed foams had interconnected structure, irregular shape and size with in a porosities range up to 52 vol. % [20].

In the hollow sphere method, the foams are sinter from preproduced hollow spheres. For the production of hollow spheres gas atomization techniques can be used. The metal is melted and gas is blown with nozzles inside the viscous metal melt drops with special techniques. During the process several polymeric or organic additives can be introduced into the metal to increase viscosity but afterwards they have to be burned. Figure 2.3 shows the Georgian Tech route of producing hollow

spheres [21]. With this technique high porosities can be achieved without pore interconnection.

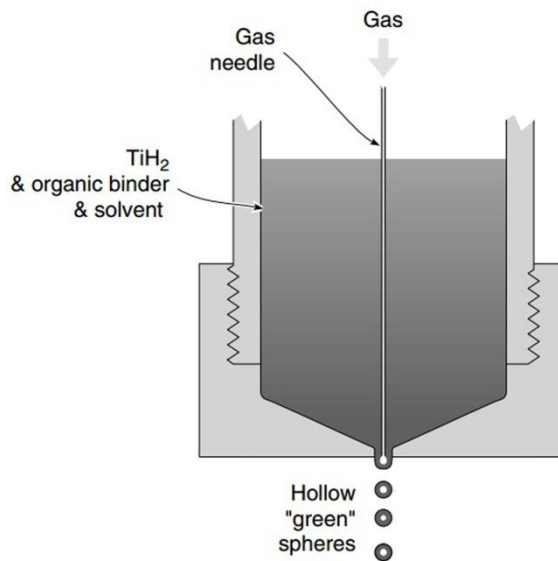


**Figure 2.3** Georgian Tech production route for hollow spheres [21].

With the replication method, highly porous open cellular foam can be produced. In order to produce metal foams first a preconstructed polymeric sponge is dipped into metal slurry and then it is heated in several stages for dehydration, burning of the polymer and sintering. In the study of Li *et al.* this technique was utilized in order to produce highly porous Ti-6Al-4V alloy. Polyurethane (PU) sponges were used in order to give shape to the metal slurry and heated to 150°C, 400°C, 500°C temperatures gradually to remove PU and then cooled to room temperature and heated to 1250°C for sintering.

Similarly, Jorgensen *et al.* used replication method to produced Ti-6Al-4V foams with porosities in the range of 20 to 35 vol. %. In this method, Ti-6Al-4V powder particles were mixed and compacted with a steel mesh. During sintering formation of Ti-Fe eutectic phase prevents Fe diffusion through Ti-6Al-4V and after sintering the steel mesh was removed electrochemically from the foam. The procedure yielded a homogenous distribution of macropores with the same size of steel wire used in the mesh [15].

### 2.2.1.1 Loose Powder Sintering

Loose powder sintering is the simplest way of producing porous structures. By this method foams with low porosity levels can be produced. In this method, metal powders are put into a mold and then sintered. The pore size and characteristics in this method can be controlled indirectly by sintering time and temperature. In addition, compaction methods can be applied to metal powder in order to decrease the porosity level by increasing contact area and breaking the stable oxide layers. Studies on aluminum foams show that prior ball milling of the powders before sintering increases the sintering ratio [18]. The pores produced with this method have irregular shape and size. A schematic description of the process and pore shapes is shown in Figure 2.4.

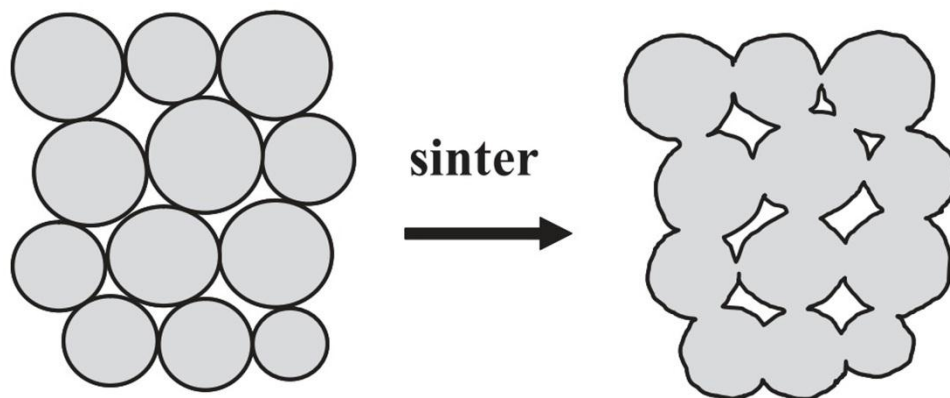


**Figure 2.4** Schematic presentation of loose powder method [19].

Studies of Esen *et al.* have shown that titanium and Ti-6Al-4V foams up to 40 vol. % porosity can be produced by use of Ti and Ti-6Al-4V powders with average sizes of 74  $\mu\text{m}$  and 107  $\mu\text{m}$ , respectively. The pores had irregular geometry varying in the size range of 10 – 100  $\mu\text{m}$ . In addition, porosity amount can be controlled and changed with sintering temperature, time and by powder characteristics [13].

### 2.2.1.2 Space Holder Technique

Highly porous foams with open and interconnected pores with desired shape can be produced by this method. The main logic of this technique is to cover the appropriate spacers with the metal powder by using a binder or solvent. After the covering step, the mixture is compacted under pressure and then sintered. During, prior to or after sintering, it is necessary for the spacer to leave the mixture system. A general route for this method is shown in Figure 2.5 [18]. For the production of highly porous titanium and titanium alloys several spacers can be used. Magnesium powders, carbamide (urea) particles, tapioca starch, ammonium hydrogen carbonate particles, salt are some of the frequently used spacers in the production of highly porous Ti and Ti alloys [22, 23, 24, 25]. Spacers used during the process have significant effect on properties and processing.

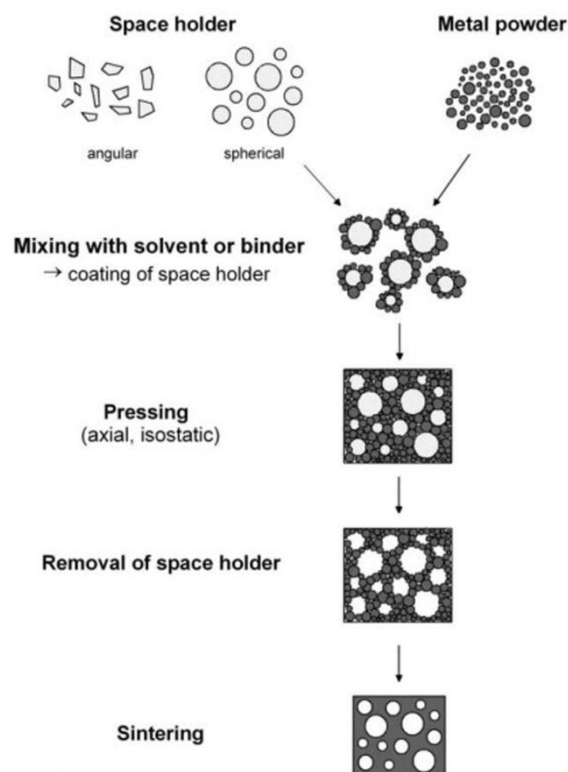


**Figure 2.5** General steps of processing foams with space holder technique adapted from Banhart *et al.* [18].

Pore characteristics are directly related to the space holder used since pores are formed when the spacer leaves the system. Therefore, porosity level, pore shape, size, geometry, distribution can be controlled by controlling those for the spacer.

In addition, the spacers also modify the processing steps of the production technique. In the studies of Sharma *et al.*, Ti foams with ~30 vol. % porosity were produced via using acicular urea particles. Before sintering, compacts were preheated to 300°C for 2 hours [24]. Due to the acicular shape of the spacers the foams were composed of acicular pores which may create stress concentrations and mechanical anisotropy. On the other hand, Mansourighasri *et al.* processed by using tapioca starch as a spacer. During the process the preheating temperature was 450°C and the foams had a final porosity between 65-80 vol. % [25]. Furthermore, Bansiddhi *et al.* used NaCl particles as spacers for the production of TiNi foams. The compacts were first sintered at two different temperatures, 950°C and 1065°C, well above the 810 °C melting temperature of NaCl, in a hot isostatic press and then the spacers were dissolved in water [26]. In another study, Esen *et al.* processed porous Ti and Ti-6Al-4V foams with a porosity range of 40-80 vol. % via employing spherical magnesium particles. During the process the compacts were directly heated to the sintering temperature in a single step without any preheating operations. Magnesium spacers melted and vaporized during the heating process. In addition, magnesium vapor created a protective atmosphere for titanium powders due to its higher reactivity with oxygen. The processed foams had spherical and interconnected pore geometry [13]. In the in-vivo studies of Arpak *et al.* bone ingrowth was observed through the porous TiNi foams produced via using magnesium spacers in the range of 250 - 600 µm [27].

### **2.3 Conventional Sintering**

Sintering of metal and ceramics powders is a common production method that has been employed from the beginning of civilization. Porous metals, structural steel parts, tungsten wires, bearings, hard magnetic materials are some of the examples in today's world which are produced by sintering of powder particles [28].

Solid state sintering is a process in which compacted powder particles are heated above approximately half of the melting temperature depending on the melting characteristics. The difference between a powder particle and a dense bulk material is the excess free energy created due to broken atomic bonds at the surface of the powder particle. Mass transfer in sintering is therefore driven by surface energy or the capillarity effect. The excess free energy or free surface increases with finer powder particle size. Sintering occurs with diffusional flow of atoms to the necks which are the contact point of the powders. The flow is from the concave surfaces where stress is tensile through the convex surface where the stress is compressive. This stress,  $\sigma$ , can be defined as;

$$\sigma = \frac{\gamma}{\rho} \quad (2.1)$$

Where  $\gamma$  is the surface energy and  $\rho$  is the neck curvature.

The flow of the atoms between two powder particles can occur by different mechanisms; surface diffusion, lattice diffusion, vapor transport, grain boundary diffusion, and plastic flow. The schematic representation of diffusion mechanisms is given in Figure 2.6 [29].

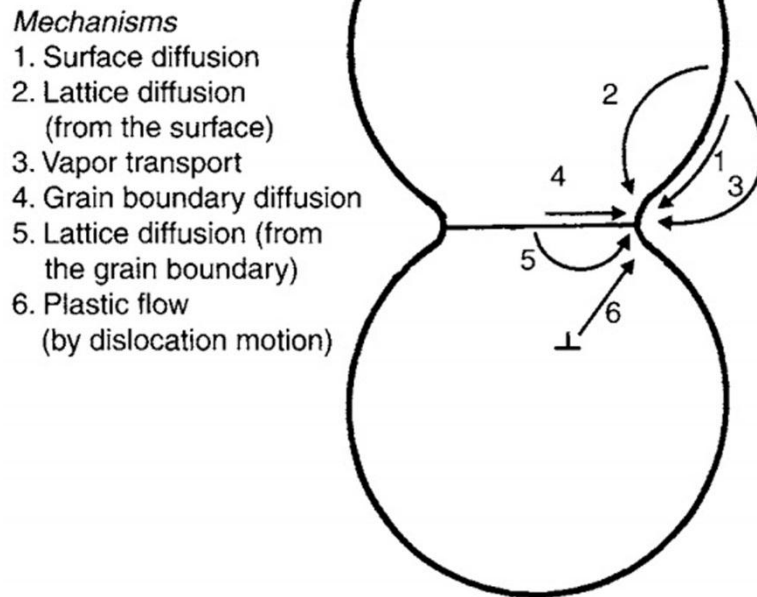


**Figure 2.6** Flow mechanisms occurring during sintering [29].

The solution for the total flow equation of atoms in a system composed of two powder particles with same size is solved according to;

$$\frac{x^n}{r^m} = A(T) \times t \quad (2.2)$$

Where  $x$  is the neck radius,  $r$  is the powder particle radius,  $A(T)$  is a function of temperature and  $t$  is time,  $n$  and  $m$  are the constants related to the dominant mass transfer types; surface, lattice, etc.

## 2.4 Mechanical Behavior of Porous Materials

### 2.4.1 Compressive Response

Under compressive loading, foams exhibit deformation characteristic different than bulk materials. They deform in three stages. At first, there is a linear macroscopically elastic region which is limited to relatively small strains of about

5 %. After yielding, stress strain curve exhibits a plateau region which can be identified with a small constant slope. Finally, a rapid stress increase known as densification is observed [17]. Figure 2.7 shows a commonly observed compressive stress strain diagram, which indicates the specific regions of deformation.

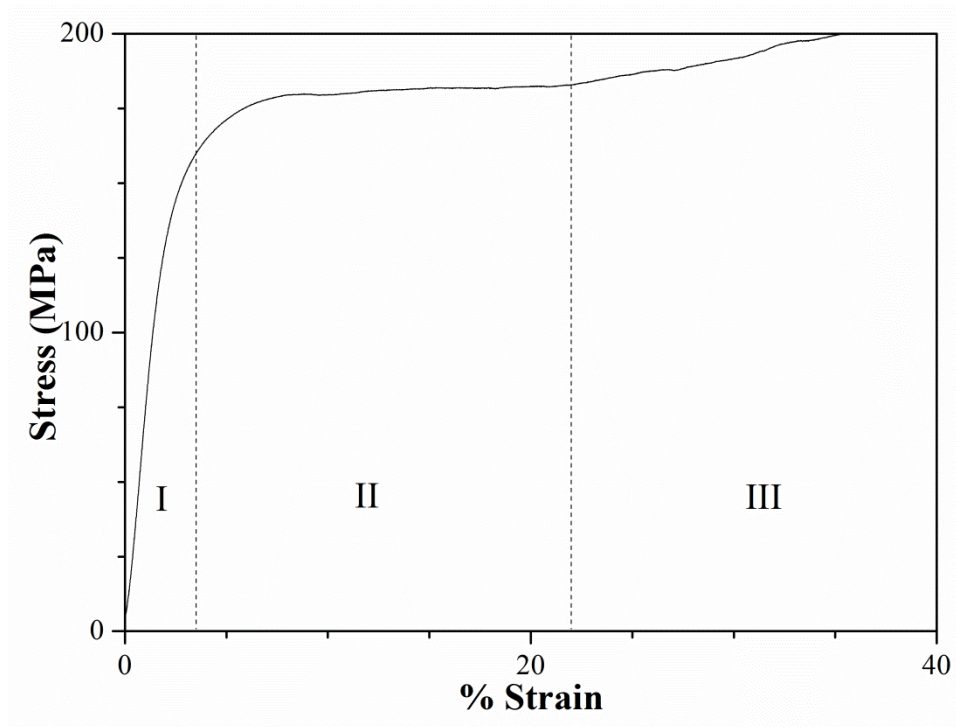


**Figure 2.7** A typical compressive stress - strain curve of foams showing general characteristic regions.

In addition to the general form of the curve, there can be stress fluctuations after the first stage of deformation as an indication of brittle fracture of cell walls [17].

The elastic deformation of the open pore structured foam occurs by bending and buckling of the cell walls [17]. Figure 2.8 shows the initial and compressive loading stages of a cuboidal open pore structure.

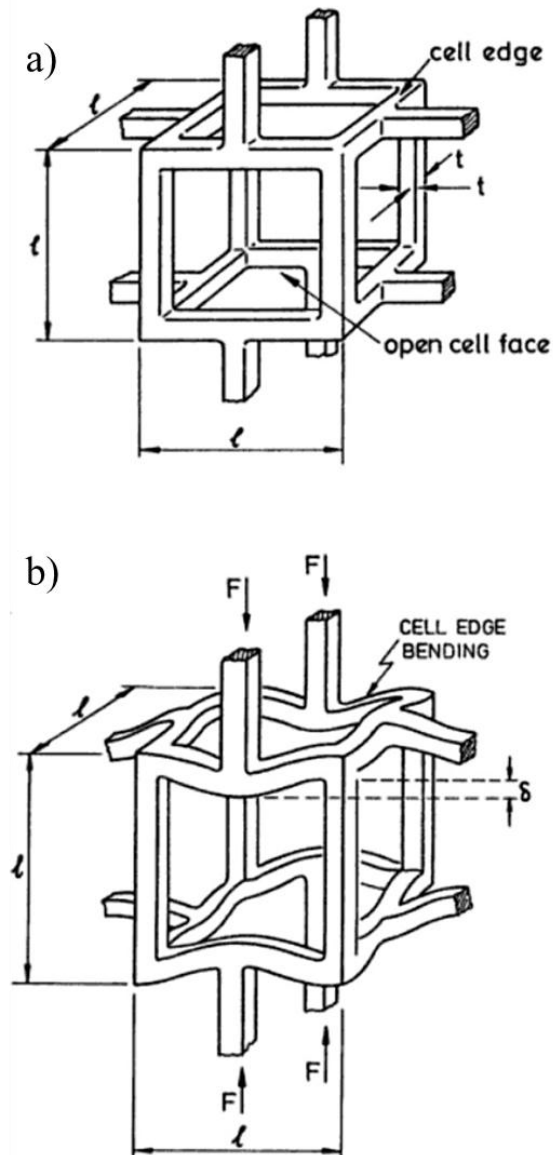


**Figure 2.8** Elastic bending and buckling of the cell walls of an open pore, a) initial state b) elastically deformed stage [17] and  $F$  showing the loading direction and points.

Plastic deformation occurs with plastic buckling and bending of cell walls after the elastic deformation regime. The slope and length of the plateau is related to the geometry of the cell walls. The plateau continues until all the cell walls are bend or buckled. Plateau is not affected from the completion of deformation of a single cell

since other cell walls continue to deform. The plateau region end when the cell walls collapses or fractures and the solid is compressing to itself.

A mathematical model for prediction of mechanical properties such as elastic modulus and yield strength, of the foams was proposed by Ashby and Gibson [30]. The solution of the model of mechanical properties of an open pore structured foam obeys a power law relationship in the form of,

$$\text{Mechanical Property of the Foam, } M = M_o \times \left(\frac{\rho}{\rho_o}\right)^n \quad (2.3)$$

Where  $M_o$  and  $n$  are constants related to the geometry, size, shape, distribution of the pores,  $\rho$  is the density of the foam and  $\rho_o$  is the density of the bulk material.

In the literature there are also micromechanical models using cell wall thickness and bending deflection as parameters in order to estimate the mechanical properties [31]. However, in order to use micromechanical models cell wall geometries should be simple. In addition, the models neglect the microporosities present in the cell walls due to insufficient sintering which results in deviations from the models.

#### **2.4.2 Fatigue Response**

Fatigue is probably the most important failure mechanism in mechanical systems since the failure occurs without any obvious macroscopic sign below a stress level much lower than the required stress for fracture. Fatigue failure is observed on materials which are exposed to cyclic loading and the failure occurs after a period of time. Nearly in all applications, system is subjected to varying loads causing fatigue. It is therefore one of the most critical properties of components in applications. Fatigue mechanism and failure has been studied extensively for bulk materials.

For fatigue failure to occur basically there should be a maximum tensile stress with sufficiently high amplitude applied for large number of cycles.

During fatigue failures in a metal free from flaws microcracks form, then they coalesce and grow to macro cracks and finally, rapid and sudden fracture occurs. The first fatigue cracks nucleate from the surface which has a higher probability of having scratches, sharp corners, pits, inclusions and stress concentrations [32].

Fatigue cracks initiate from regions with high localized stresses present due to surface defects, notches or inclusions. Even in the absence of localized stresses, a slip plane remains which cannot be cancelled during the cycles remains in the material. These slip planes, which cannot be cancelled, creates slip accumulations. The accumulated slip bands forms intrusions and extrusions. The mechanism of the formation of intrusions and extrusions is not clear. Cottrell and Hull suggested that intrusions and extrusions were formed by sequential slip on two intersecting slip planes and Neuman proposed that they can be formed by dislocation avalanche along parallel neighboring slip planes containing dislocation pile ups of opposite signs [32, 33, 34]. Fatigue cracks initiate from these sites and grow. A schematic representation of intrusion and extrusions is shown in Figure 2.9.

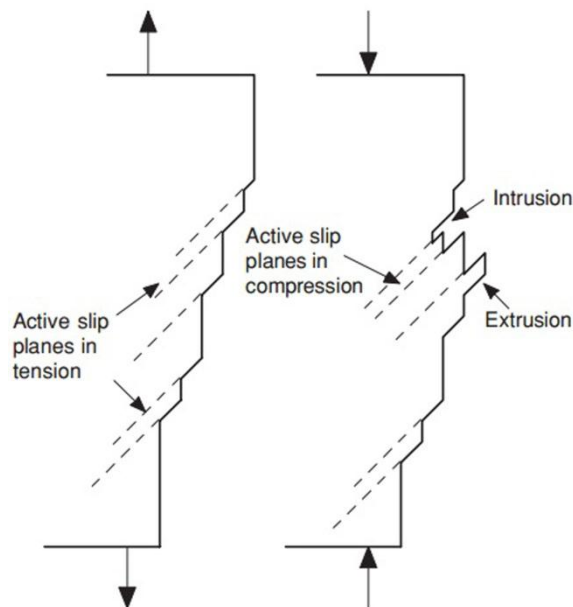


**Figure 2.9** A schematic representation on the formation of intrusions and extrusions. The arrows show direction of the loading [35].

The growth of fatigue cracks are divided into two stages. In the first stage the crack grows through slip planes for three or four grain size. In the second stage growth becomes perpendicular to the loading axis until fracture toughness is exceeded and fracture occurs [36].

For comparing fatigue behavior of materials stress – number of cycles diagrams (S-N) can be used. These diagrams may be drawn according to stress amplitude,  $\sigma_a$ , stress range,  $\sigma_r$ , mean stress,  $\sigma_m$ , or maximum applied stress,  $\sigma_{max}$ . The definitions of the stress terms are shown in Figure 2.10.

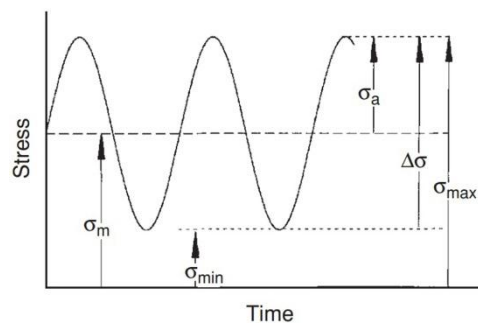


**Figure 2.10** Definitions of the stress terms [35].

In addition to S-N curves, strain - number of cycle curves are drawn in order to investigate the change of response to the load. As shown in Figure 2.11 strain - number of cycle curves for metallic foams under compression fatigue is divided into three stages [37].

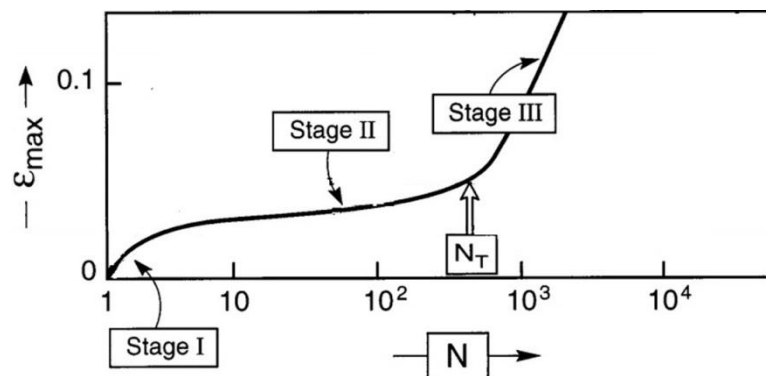


**Figure 2.11** Change of strain with respect to number of cycles in compression compression fatigue [37].

In the first stage strain accumulates due to early formation of cracks. In the second stage the accumulated strain does not change too much. This period can be called incubation period for crack growth. In the final stage the strain increase rate increases rapidly and failure occurs [37]. This final stage is observed in three different ways. The first type of failure occurs with uniform accumulation of strain through the foam. There is no formation of crush bands or localized failures. The failure happens in a single and sudden step. This type of failure is observed in DuocelfoamsAl-6101-T6 [21].

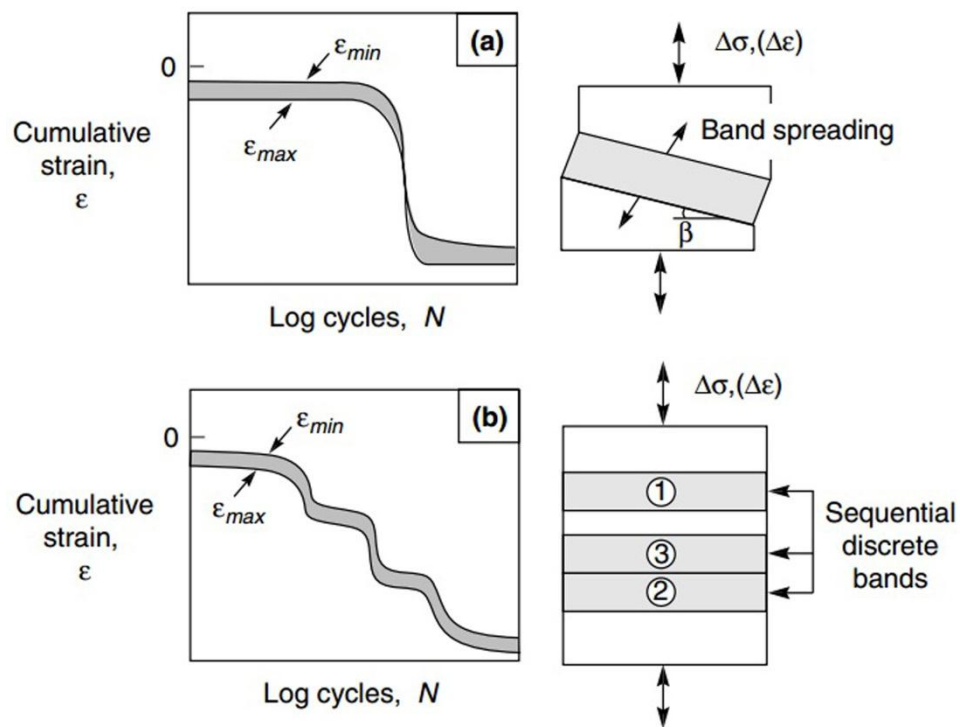


**Figure 2.12** Typical behaviors of foams under compression loading. (a) Failure occurs with broadening of a single crush band, (b) Failure occurs with broadening of multiple crush bands [38].

The second type of failure behavior is shown in Figure 2.12.(a). Deformation starts from the weakest cell wall and creates a crush band. This single crush band broadens leading to failure. This type of failure is observed on Alulightfoams of composition Al – 1Mg – 0.6Si (wt. %) [38].

The third type of failure behavior is shown in Figure 2.12.(b.) In this behavior multiple crush bands are formed from the weakest sections of the foams. Strain accumulation increases up to failure of a single crush band. The formed crush bands fail one by one with each failure creating a strain accumulation step. This type of failure is observed in Alcan Al – SiC foams [38].

## CHAPTER 3

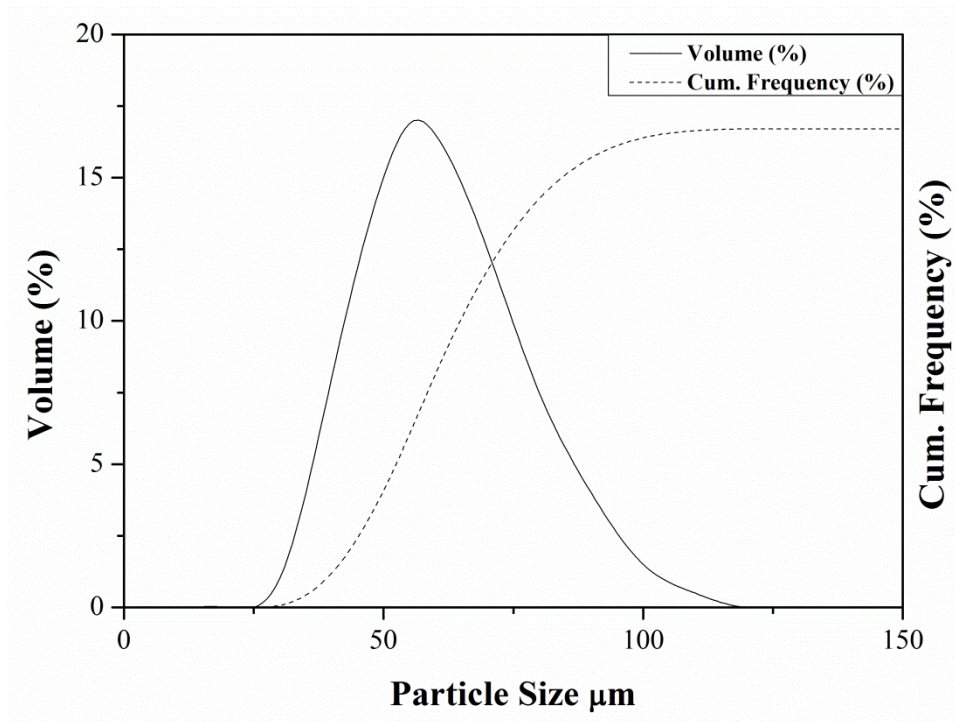
### EXPERIMENTAL PROCEDURE

#### 3.1 Powders Used

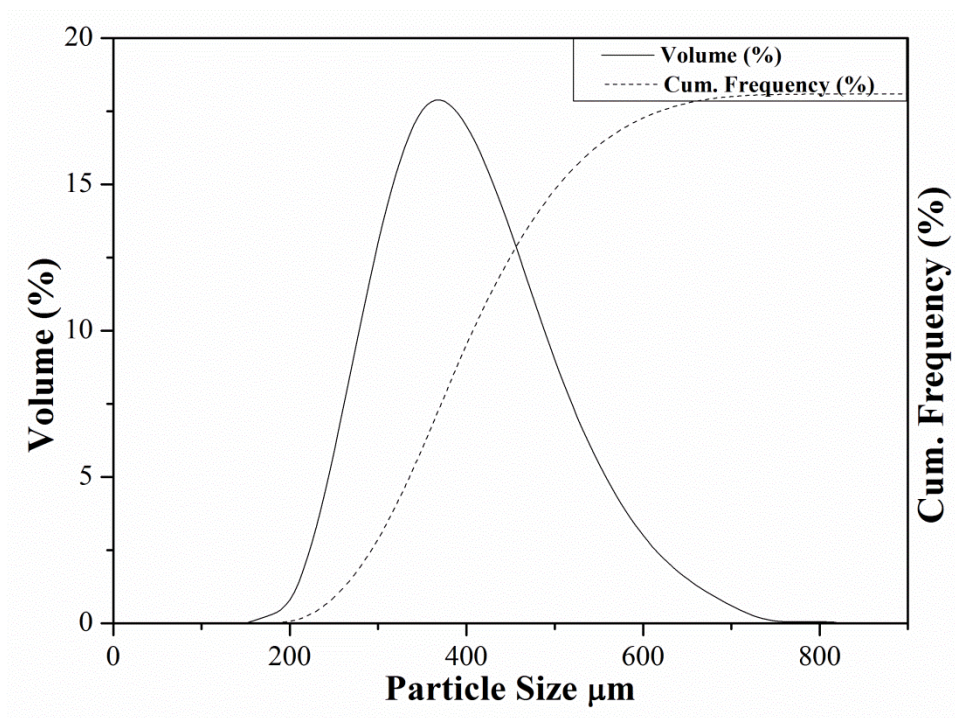
In the present study, spherical Ti-6Al-4V powders (ASTM F1580-01, Phelly Materials Inc., New Jersey, U.S.A) were used for the production of porous Ti-6Al-4V foams. The prealloyed powders were used to prevent formation of oxide inclusions and ternary phases, and composition variations.

Magnesium (Mg) powder (99.82 % purity, TangShanWeiHao Magnesium Powder Co. LTD., Tangshan, Hebei Province, China), was used in the production of Ti-6Al-4V foams. Magnesium was chosen as space holder material not only for its low evaporation temperature and higher oxygen affinity but also for its low Ti solubility. Magnesium vapor prevents the oxidation of Ti-6Al-4V alloy during sintering at 1200°C by reducing the oxygen present in the atmosphere and also reduces the oxide layer present on the surface of Ti-6Al-4V alloy without dissolving in the alloy. The size and shape of the Mg powders are directly related to the final size and shape of the macropores in the Ti-6Al-4V foam. Powders were chosen to be spherical to minimize stress concentrations. Magnesium powders were sieved to the range of 250-600  $\mu\text{m}$  in order to have pore size distribution suitable for biomedical applications in the Ti-6Al-4V foam produced.

Both Ti-6Al-4V and Mg powders used in this study exhibited Gaussian distribution with average particle sizes of  $\sim 55$  and  $\sim 375$   $\mu\text{m}$ , respectively (Figure 3.1).



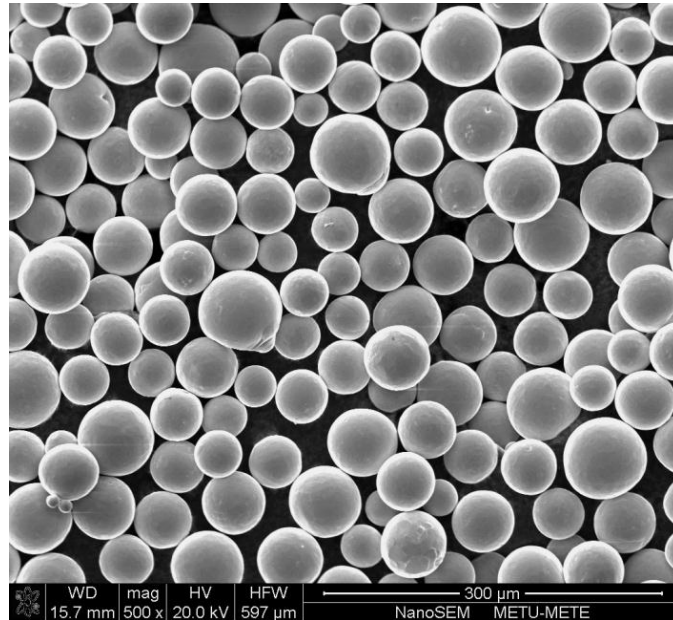
(a)



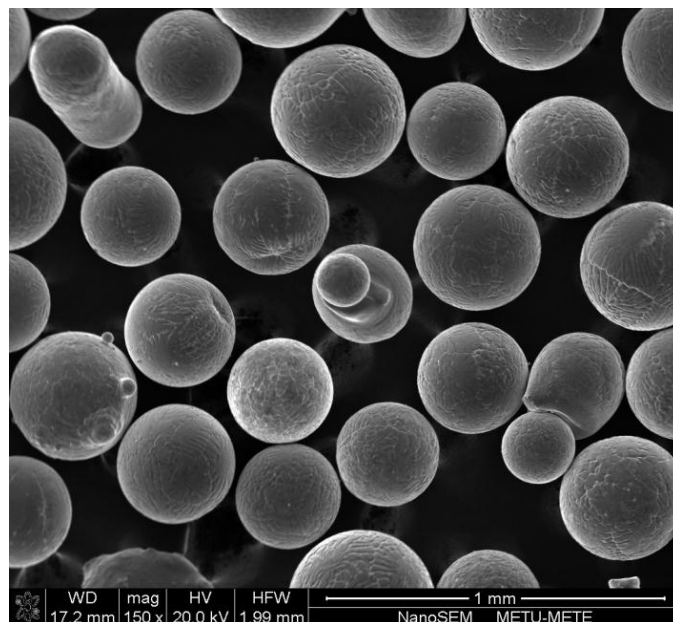
(b)

**Figure 3.1** Particle size distribution of (a) Ti-6Al-4V, (b) Mg powders. Solid lines represent volume percentages and dashed lines show cumulative frequency percentages.

Morphologies and size distributions of both Ti-6Al-4V and Mg powders employed, which were produced by gas atomization technique, were investigated under scanning electron microscope (Nova Nano SEM 430, FEI LTD, Oregon, USA) (Figure 3.2).



(a)



(b)

**Figure 3.2** SEM micrographs of (a) Ti-6Al-4V, (b) Mg powders.

X-ray diffraction analysis (Rigaku D/Max 2200/PC, Rigaku Corporation, Tokyo, Japan) of Ti-6Al-4V powders conducted by 40kV Cu X-ray source in the range 20° to 90°, showed only the presence of  $\alpha$  phase (ICDD #44-1294). The diffractogram in Figure 3.3 shows the x-ray diffraction pattern of the as-received Ti-6Al-4V powders.

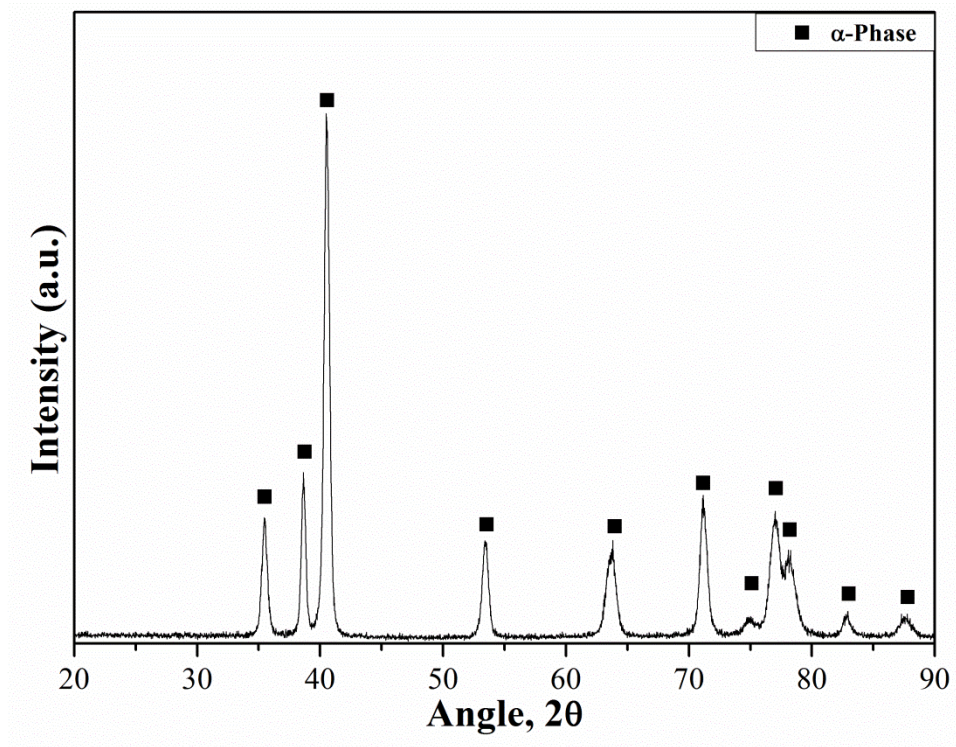


**Figure 3.3** X-ray diffractogram of the as received Ti-6Al-4V powders.

### 3.2 Production of Porous Ti-6Al-4V Alloys

Macro porosities of Ti-6Al-4V foams were formed and adjusted by addition of Mg as space holder material. Ti-6Al-4V powders were mixed with Mg powders at the desired amount (50-70 vol. % for the present study) and 5 wt. % polyvinyl alcohol solution (2.5 wt. % PVA+ distilled water) was used as binder. The amount of binder was crucial for covering the surface of the powders and forming a homogenous mixture. The mixture was blended homogeneously until all the PVA solution covered the powders and the excess water in the PVA solution got evaporated. It

was important for the blend to be in the particular wetness which was the point just before dissociation of the Ti-6Al-4V powders from Mg powders. Over or under mixing caused cracks in the compacts during compaction stage. In case of under mixing, compacts fractured from the middle due to presence of incompressible liquid in the mixture which causes expansion of the compact when the load was released. In the other case, green strength of the compacts was too low and handling of the compacts was impossible. It was observed that a mixing time of approximately 20 minutes was suitable for the powder mixtures to be in the proper condition form before compaction. In addition to mixing time, friction between the die and the powders was another important criterion for preventing compact cracking in compaction stage. In order to reduce die wall friction zinc stearate powder was used as lubricant on the inner surface of the die. Powder mixture were compacted in a double-ended steel die under 500 MPa pressure by using hydraulic press to attain cylindrical compacts with an aspect ratio of 1 (Figure 3.4).

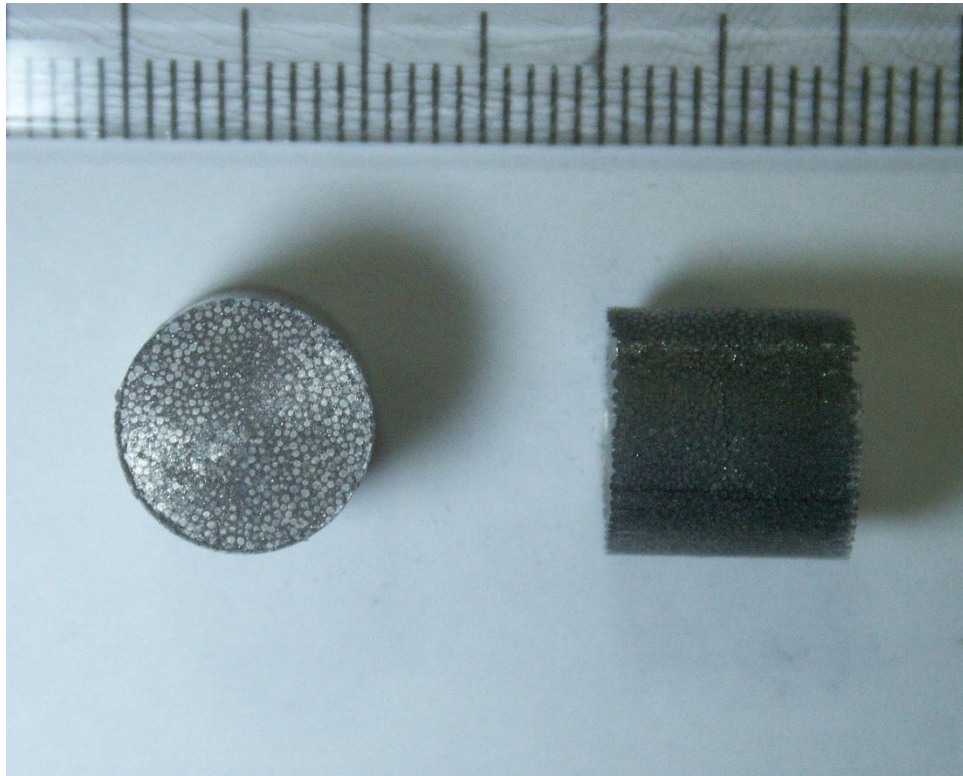


**Figure 3.4** Cold pressed Ti-6Al-4V and Mg mixture compacts. The white and bright regions are Mg powders and grey regions are Ti-6Al-4V powders.

Compacts of Ti-6Al-4V/Mg powder mixtures were sintered in a vertical tube furnace under high purity argon (99.999% purity, N<sub>2</sub>: 6.2vpm, O<sub>2</sub>: 2.2 vpm, humidity: 2vpm) atmosphere at 1200°C for 2 hours.

For the sintering process, compacts were placed into Ti-6Al-4V crucibles. A schematic cross sectional view of the crucible is shown in Figure 3.5. The crucible material was chosen as Ti-6Al-4V due to its chemical stability under Mg vapor, which is produced upon the evaporation of Mg powders during sintering. MgO pellets, produced from MgO powder compacted at 100 MPa and sintered at 1200°C, were placed to the bottom of the crucibles to avoid contact and diffusion between the crucible and the foam. The compacts were placed on top of previously used scrap Ti-6Al-4V foam put onto the MgO pellets to prevent the long term contact of liquid Mg and allow the flow of liquid Mg completely out of the specimen during the heating process. Additionally, Ti sponges were placed on top of the crucibles as oxygen getters assisting Mg vapor. However, in most cases sponges were unoxidized, showing that the Mg vapor present in the furnace was sufficient to avoid oxidation.

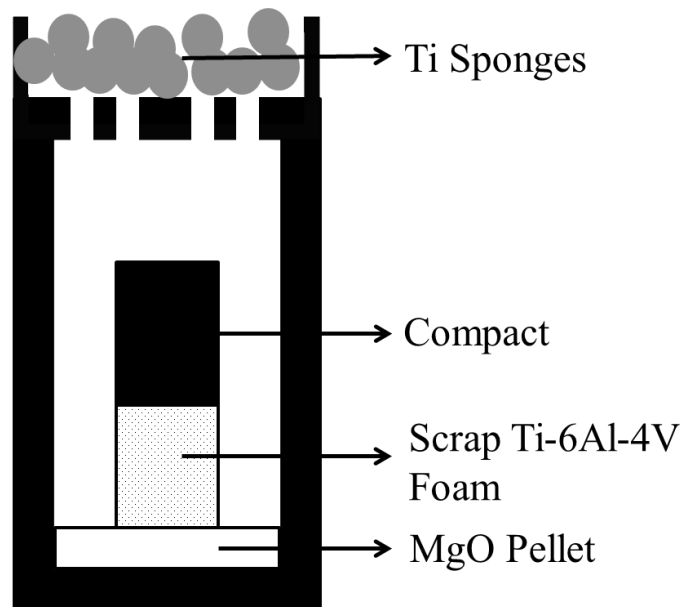


**Figure 3.5** Cross section of the crucible.

The crucible was lowered to the predetermined hot zone of the furnace. It was important for the crucible not to touch the alumina tube of the furnace to avoid unwanted reactions. Prior to heating the furnace was purged with high purity argon for ten minutes to reduce the amount of oxygen in the furnace before the heating started. The furnace is heated up to  $1200 \pm 5^\circ\text{C}$  with  $10^\circ\text{C}/\text{min}$  heating rate. Heating rate of the furnace was adjusted to prevent collapse of the compacts during melting of the Mg powder. The compacts were sintered for 2 hours and cooled inside the cold zone of furnace. To avoid oxidation and for proper cooling, processed foams were kept in the furnace until the hot zone temperature drops below  $450^\circ\text{C}$ . Figure 3.6 shows the summary of the production steps used in this study.

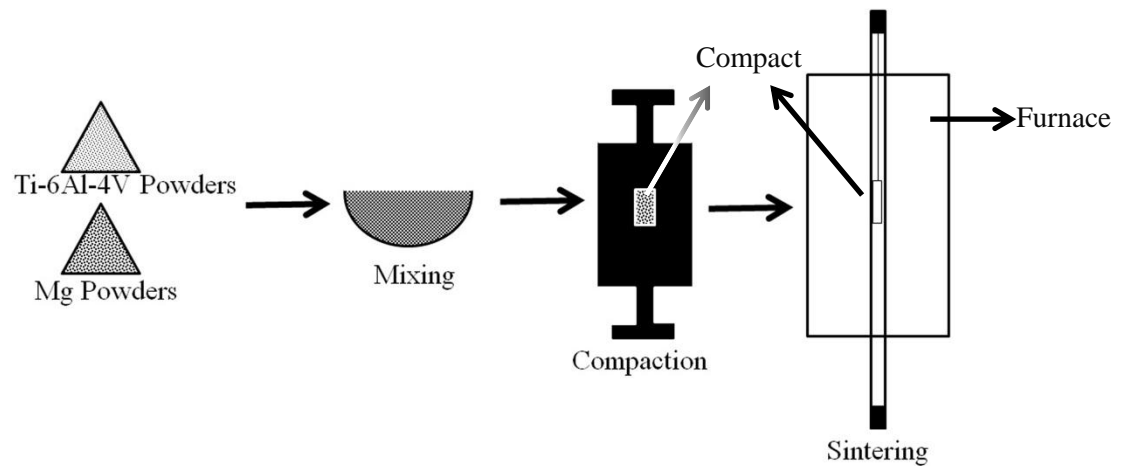


**Figure 3.6** Representative steps of foam processing with Mg space holder method.

### 3.3 Characterization Studies

#### 3.3.1 Particle Size Distribution

Particle size distribution analysis of the Ti-6Al-4V and Mg powders was done by Malvern Mastersizer 2000 Particle Size Distribution (PSD) Analyzer, which is capable of measuring particle sizes in the range of  $0.02\text{-}2000\ \mu\text{m}$  with an accuracy of  $\pm 1\%$ .

### 3.3.2 Density and Porosity Measurements

Density and porosity measurements of the produced Ti-6Al-4V foams were done according to Archimedes principle which correlates the weight of the immersed object to the volume of the displaced fluid. Precision balance (CP224S-0CE, Sartorius, Goettingen, Germany) equipped with a density measurement kit was used for the density calculations. The procedure for the measurement of the density is given below,

1. The weight of the foam ( $W_{\text{foam}}$ ) was measured and then immersed into the xylene ( $\text{C}_6\text{H}_4(\text{CH}_3)_2$ ) solution.
2. To ensure that the xylene solution fill all the pores, the foam was put into a beaker and vacuum was applied by rotary pump for one hour.
3. The weight of the foam ( $W_{\text{foam in xylene}}$ ) was measured in xylene solution.
4. The weight of the xylene impregnated foam ( $W_{\text{foam with xylene}}$ ) was measured in air.

The bulk density of the Ti-6Al-4V foam was calculated according to Equation 3.1, where density of xylene is  $0.861 \text{ g/cm}^3$  and density of Ti-6Al-4V alloy is  $4.42 \text{ g/cm}^3$ .

$$\frac{\rho_{\text{foam}}}{\rho_{\text{xylene}}} = \frac{W_{\text{foam}}}{W_{\text{foam with xylene}} - W_{\text{foam in xylene}}} \quad (3.1)$$

The amount of total porosity fraction ( $P_{\text{tot}}$ ) was calculated with the equation:

$$P_{\text{tot}} = 1 - \frac{\rho_{\text{foam}}}{\rho_{\text{Ti-6Al-4V}}} \quad (3.2)$$

For the determination of the open ( $P_{open}$ ) and closed ( $P_{close}$ ) porosity fractions Equation 3.3 and 3.4 were utilized.

$$P_{open} = \frac{\frac{W_{foam\ with\ xylene} - W_{foam}}{\rho_{xylene}}}{\frac{W_{foam\ with\ xylene} - W_{foam\ in\ xylene}}{\rho_{xylene}}} \quad (3.3)$$

$$P_{close} = P_{tot} - P_{open} \quad (3.4)$$

In addition, cell wall densities of the foams were determined by using metallographic techniques. SEM micrographs showing only the cell walls were processed by digital imaging techniques and porosity calculations were done using binary images with ImageJ program.

### 3.3.3 X-ray Diffraction Analysis

For determination of the phases present at room temperature, x-ray diffraction analyses were done on as-received powders and sintered foams by using a conventional diffractometer (Rigaku D/Max 2200/PC, Rigaku Corporation, Tokyo, Japan). The analyses were carried out with Cu-K $\alpha$  radiation operating at 40kV between 20° and 90° with a rotation speed of 2°/min.

### 3.3.4 Scanning Electron Microscopy Studies

SEM studies were conducted to investigate the morphologies of the powders, phases present, phase morphologies of the foams and fracture surfaces of the mechanically tested samples by a field emission SEM (Nova Nano SEM 430, FEI LTD, Oregon, USA) equipped with EDX analyzer system. Powders and foam/pore geometries were investigated by directly sticking the specimens on carbon tape. The microstructural examinations of the processed Ti-6Al-4V foams were done on specimens embedded into bakelite or epoxy resin and etched with 17 ml H<sub>2</sub>O: 2ml HNO<sub>3</sub>: 1 ml HF solution at room temperature.

### **3.3.5 Mechanical Characterization**

Mechanical characterizations of the produced Ti-6Al-4V foams were done by monotonic compression tests and fatigue tests in compression-compression mode in order to determine the critical mechanical parameters. The test specimens with an aspect ratio of 1 were grinded up to 1200 grid emery paper to ensure the surface smoothness and parallelism.

#### **3.3.5.1 Monotonic Compression Tests**

Compression tests were conducted on processed foams in order to determine the mechanical properties under quasi-static compressive conditions. The compression tests were carried out at a crosshead speed of 0.1 mm/min with 100kN capacity screw driven electromechanical testing machine (Instron 5582, Instron Co. LTD., Norwood, USA) at room temperature. Strain data were collected by video extensometer (Instron 2663-821, Instron Co. LTD., Norwood, USA) attached to the testing machine.

A representative compressive stress strain curve is given in Figure 3.7., on which the descriptions of the mechanical properties are also shown. Elastic moduli of the foams were calculated from the slope of the linear section of the curve. Yield strength of the foams was calculated by the 0.2 % offset method. Since the foams exhibited a densification stage, maximum strength of the foams was calculated from the deviation point of the stress strain curve from the linear line drawn through the plateau region.

For calculation of the average mechanical properties five samples were tested from each of the 50, 60, 70 vol. % Mg added foams. In addition, two samples with intermediate porosities (55, 65 vol. % Mg added) were tested for better statistics for the relationship between foam's porosity and relative density.

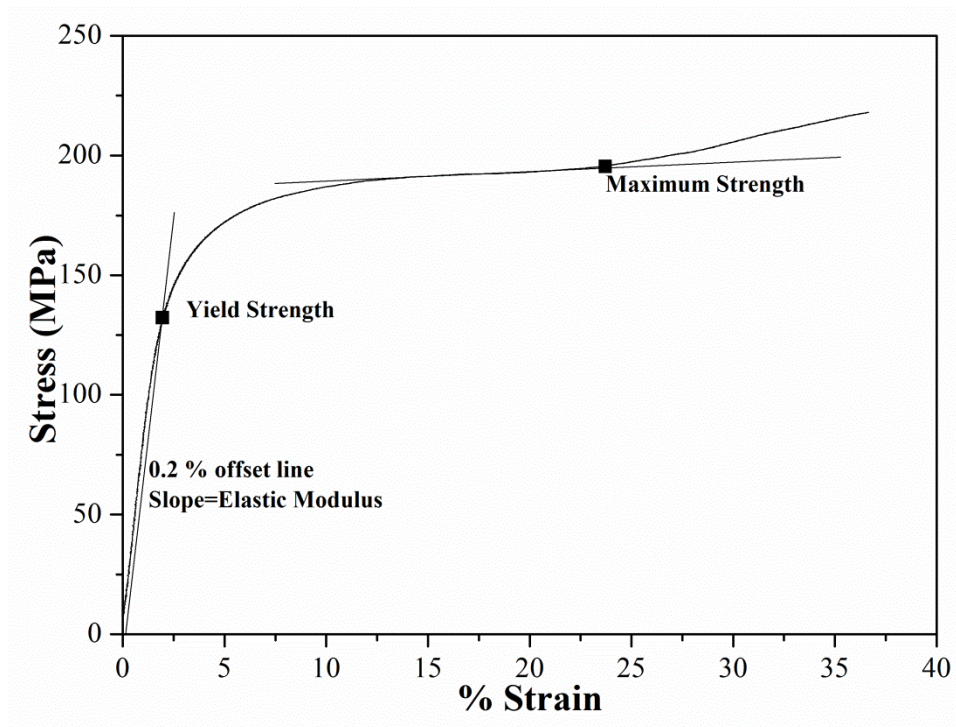


**Figure 3.7** Representative stress-strain curve of foams.

### 3.3.5.2 Fatigue Tests

Processed foams were fatigue tested under compression-compression mode. This fatigue mode was chosen since foams would generally be exposed to cyclic compressive loading when implanted in the body. Fatigue tests were conducted on the foams with 50, 60, 70 vol. % Mg additions. The tests were conducted with 5 Hz. frequency with 250kN capacity servo-hydraulic testing machine (Dartec 9500, Dartec Co. LTD., Stourbridge, West Midlands, England). The stress ratio ( $\sigma_{\max}/\sigma_{\min}$ ) was kept constant at 0.1. The yield strength was found by monotonic compression test as described in Section 3.3.5.1. For practical reasons the foams which do not fail in  $10^6$  cycles were considered as fatigue immune.

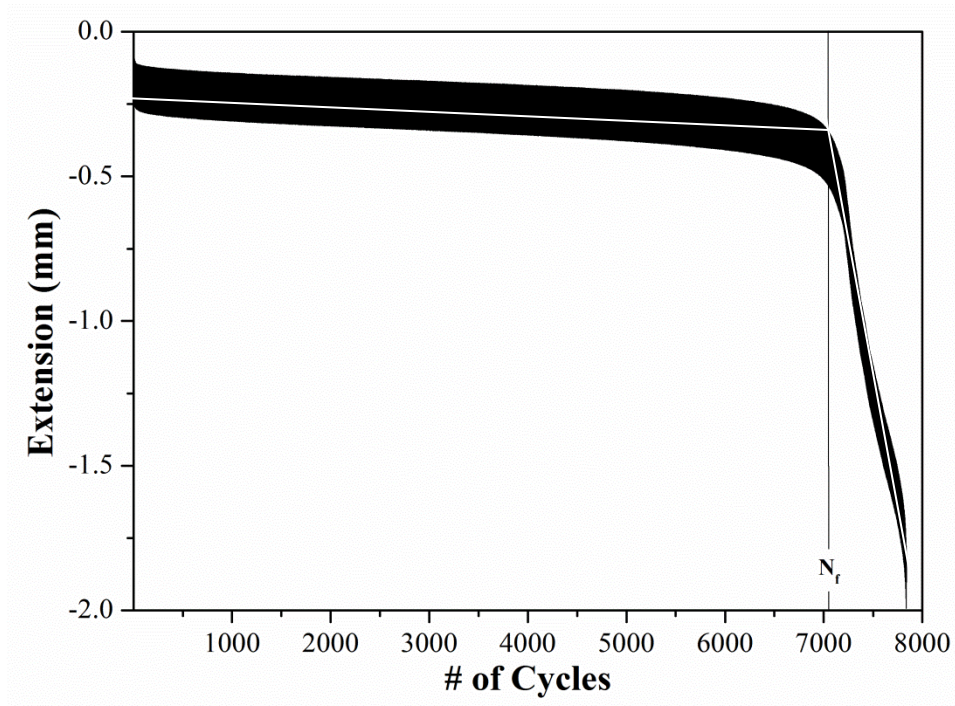


**Figure 3.8** A representative contraction - number of cycles curve obtained during fatigue testing.

A representative contraction - number of cycles curve obtained during fatigue testing is shown in Figure 3.8. Number of cycle at which failure occurs, may be defined in various ways such as knee, end of linear region, etc. The most widely used definition which is commonly accepted is the intersection of the line that fits to fast failure region with the line passing through the middle of the straight region. S-N curves were constructed using the maximum applied stress and the corresponding  $N_f$  determined as described above.

## CHAPTER 4

### RESULTS AND DISCUSSION

#### 4.1 Porosity and Pore Characteristics

Ti-6Al-4V alloy powders were compacted under 500 MPa pressure with double ended steel die by using hydraulic press to attain cylindrical shape with an aspect ratio of 1 and sintered at 1200°C for 2 hours under high purity argon gas (99.999% pure) atmosphere. Porosity contents and the densities of the foams processed using spherical Ti-6Al-4V alloy powders (~55µm) by employing magnesium space holder technique are given in Table 1 and Figure 4.1. Porosity contents, including open and closed porosity percentages, were calculated according to Archimedes' principle by using xylene solution.

**Table 4.1** Porosity characteristics of the foams.

	<b>50 Vol. % Mg</b>	<b>60 Vol. % Mg</b>	<b>70 Vol. % Mg</b>
<b>Total Porosity (%)</b>	51.14 ± 0.99	59.13 ± 0.86	64.81 ± 1.60
<b>Open Porosity (%)</b>	50.63 ± 0.98	58.54 ± 0.85	64.16 ± 1.58
<b>Close Porosity (%)</b>	0.51 ± 0.01	0.59 ± 0.01	0.65 ± 0.02
<b>Density (gr/cm<sup>3</sup>)</b>	2.16 ± 0.04	1.75 ± 0.04	1.56 ± 0.07

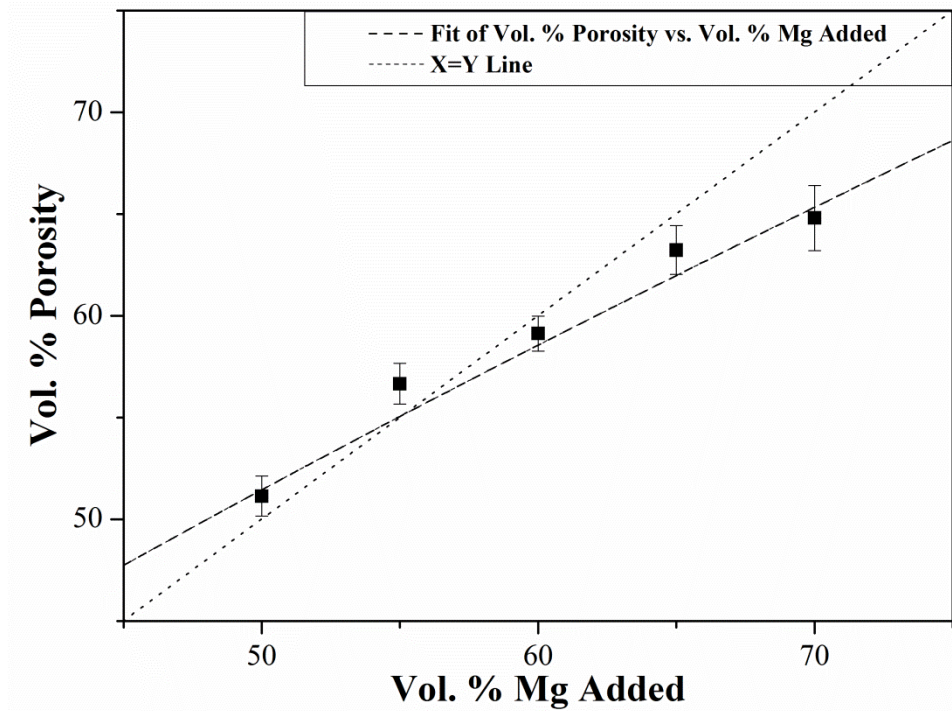


**Figure 4.1** Change of porosity with Mg addition.

Porosity calculations showed that percent porosities of the processed foams were different from the added Mg content. The change of porosity with Mg addition was found to be obeying power law relationship in the form of Equation (4.1).

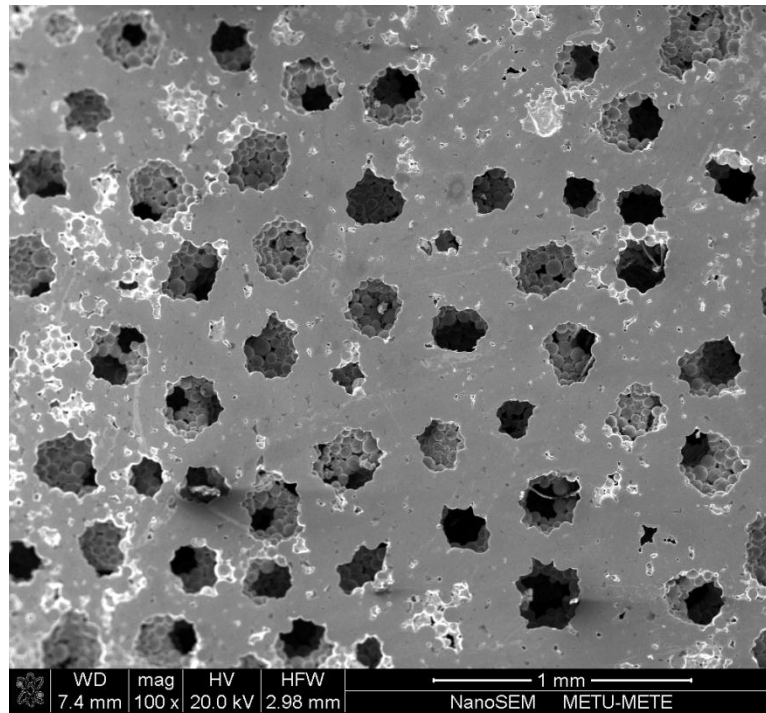
$$\text{Vol. \% Porosity} = 3.2x (\text{vol. \% Mg})^{0.71} \quad R^2 = 0.96 \quad (4.1)$$

For the present study addition of ~57 % of Mg by volume was a critical amount that vol. % of porosity obtained is equal to vol. % of Mg added prior to processing. Above the critical level processed foams resulted in porosities lower than the added spacer amount. This was attributed to the shrinkage and collapse of macropores present in the foams during the sintering process, where Mg powders melt (at ~650°C) and leave the compact by leaking out of it to create macropores. However, at that temperature Ti-6Al-4V powders hadn't sintered enough to maintain rigidity of the structure. As a result of lack of rigidity, some of the constituted macropores, which were prior Mg powder sites, collapsed. This limited amount of collapse creates enough strength for the foam being sintered to retain the rest of the structure. The amount of collapse for the structural integrity increases with

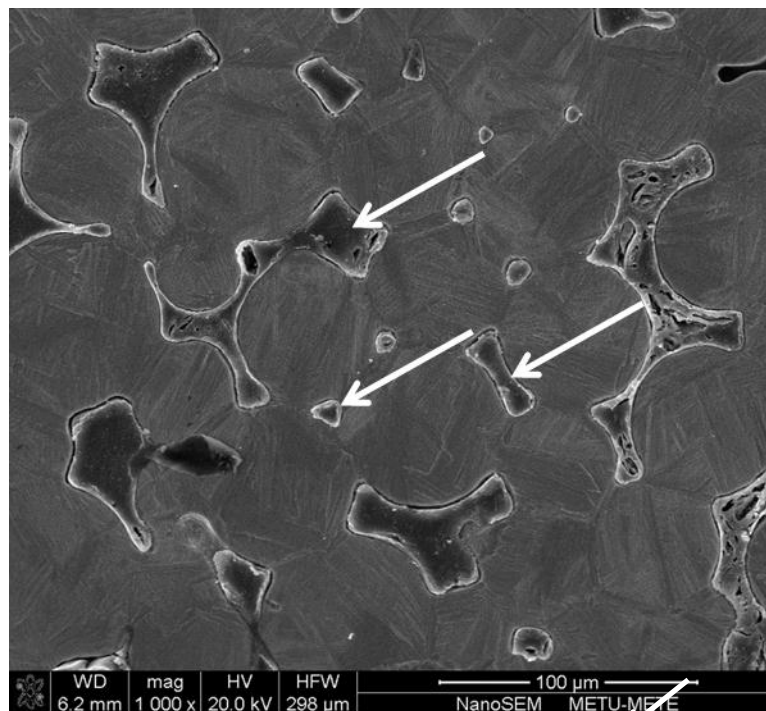
increasing porosity content. Contribution of micropores to overall porosity remains negligible with respect to the collapse of the macropores. In contrast, below the critical level, total porosity of the processed foams was higher than the added spacer amount due to the presence and contribution of micropores. The collapse of macropores was negligible for the processed foams below the critical porosity level since thicker cell walls or struts had enough strength to carry the foams weight and interconnection of macropores rarely observed. However, the presence of micropores due to insufficient sintering increased the final porosity percentage.

In addition, cell wall densities of the foams were constant for all samples containing different amount porosity and it was calculated by using SEM micrographs as  $3.71 \pm 0.06 \text{ g/cm}^3$  which corresponds to  $16.2 \pm 1.3 \text{ vol. \%}$  porosity.

Foams produced showed two types of pore structures, namely, macropores (Figure 4.2.(a)) and micropores (Figure 4.2.(b)). Macropores which were produced by the melting and evaporation of Mg spacers, had roughly spherical shape and interconnected structure (Figure 4.2.(c)). The shape, size and amount of macropores were directly related to those of Mg spacers. On the other hand micropores were residual porosities left between Ti-6Al-4V powders due to insufficient sintering because of relatively low sintering temperature,  $1200^\circ\text{C}$  corresponding  $0.78T_m$  of Ti-6Al-4V alloy.

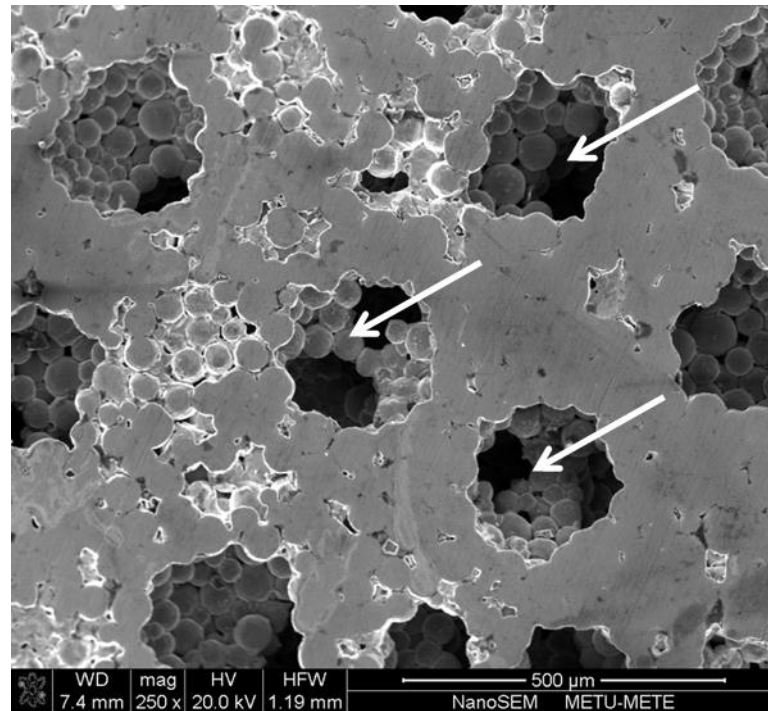


(a)



(b)

**Figure 4.2** SEM micrographs showing (a) macropores, (b) micropores, (c) interconnected macropores.



(c)

**Figure 4.2 (cont.)** SEM micrographs showing (a) macropores, (b) micropores, (c) interconnected macropores.

#### 4.2 X-ray Analysis and Microstructure

X-ray diffraction analyses were conducted to the processed foams in order to identify phases present in the processed foams. The phases were named with respect to  $\alpha$  and  $\beta$  phases of pure titanium since the substitutional Al and V atoms only shift peak positions. The X-ray diffractograms of the foams showed that the foams were composed of  $\alpha$  phase (HCP) (ICDD #44-1294) and small amount of  $\beta$  phase (BCC) (ICDD #44-1288) (Figure 4.3). On the other hand, there were no sign of formation nitride, hydride or oxide phases including Ti and Mg oxides. The presence of especially  $\text{TiO}_2$  would degrade the mechanical properties of the processed foams significantly.

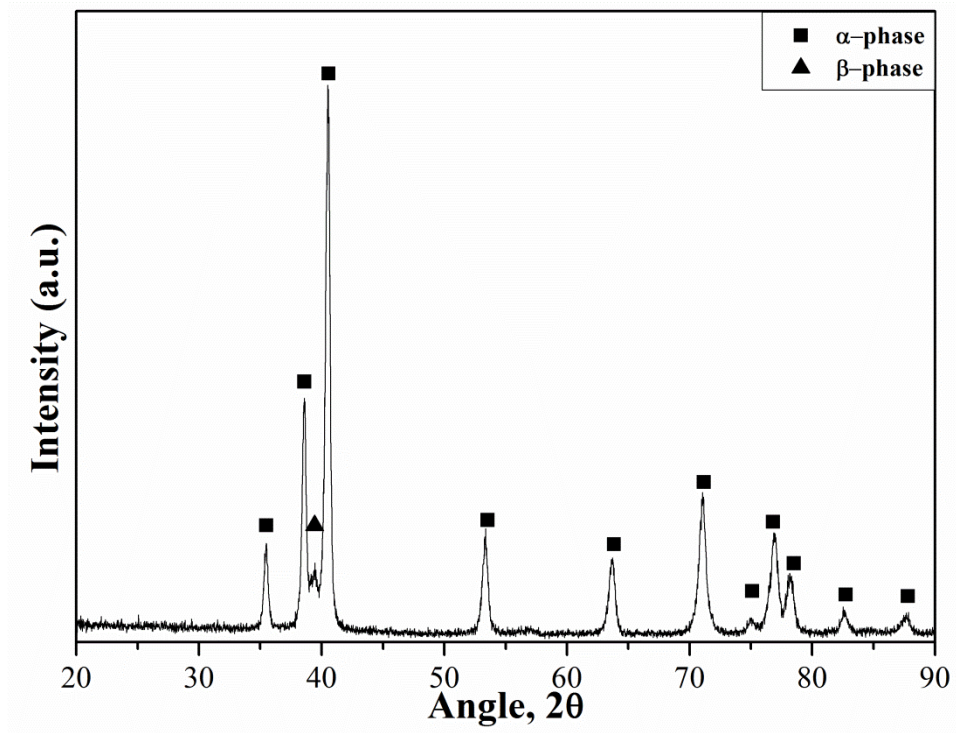
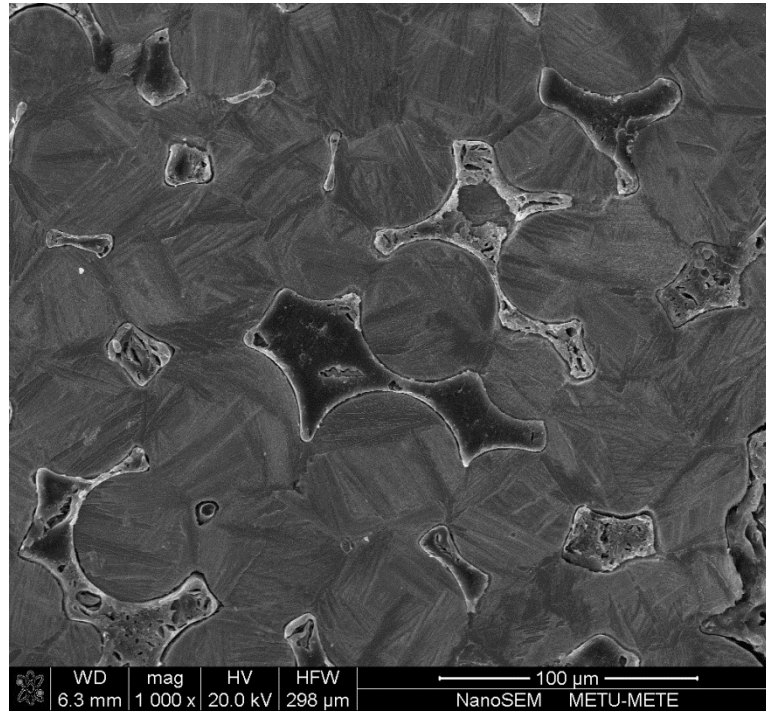
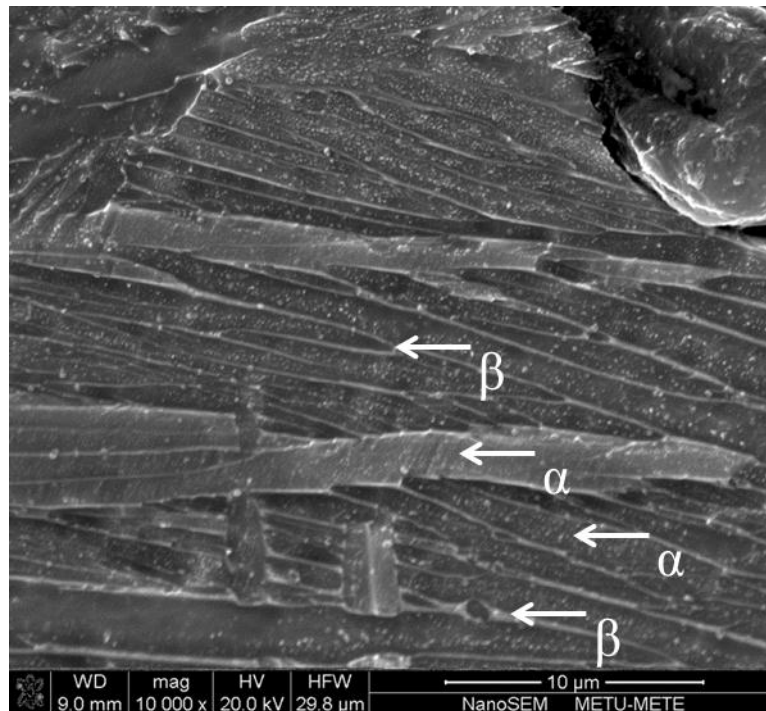


**Figure 4.3** X-ray diffraction Analysis of produced foams.

Cooling of Ti-6Al-4V foams from sintering temperature of 1200°C to room temperature in the cold zone of vertical tube furnace resulted in a lamellar type Windmanstätten microstructure. As shown in SEM micrograph (Figure 4.4), the thick dark regions and thin bright regions correspond to  $\alpha$  and  $\beta$  phases, respectively. The thicknesses of  $\alpha$  and  $\beta$  phases play a crucial role in determining mechanical properties as well as the colony size. The thicknesses of  $\alpha$  laths and  $\beta$  plates were measured as 1.30  $\mu\text{m}$  and 0.18  $\mu\text{m}$  respectively.



(a)



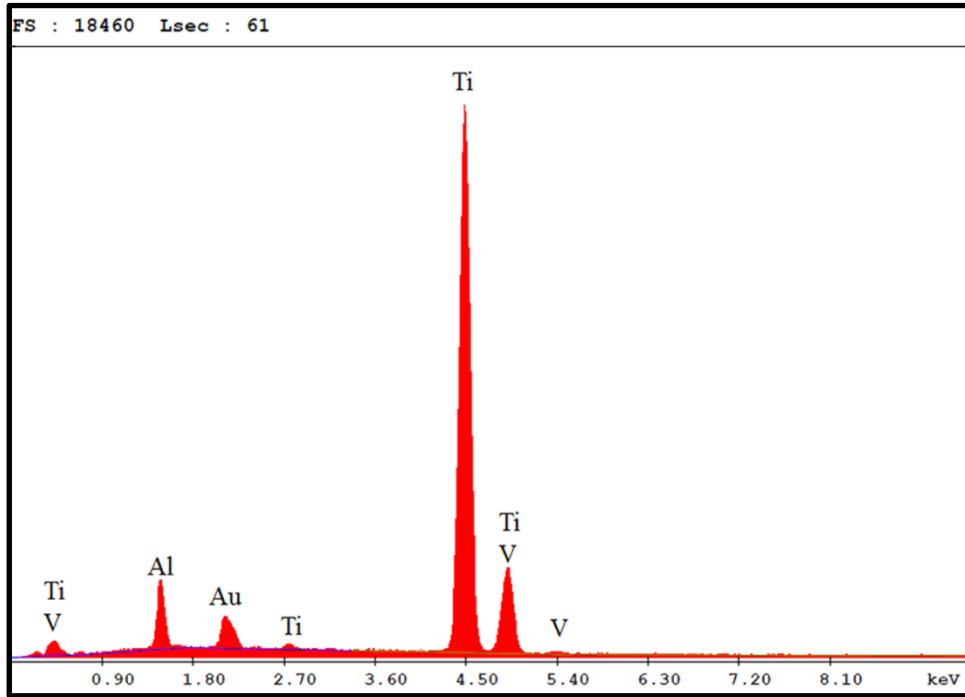
(b)

**Figure 4.4** SEM micrographs of the microstructures present in the produced foams (a) 1000x, (b) 10000x.

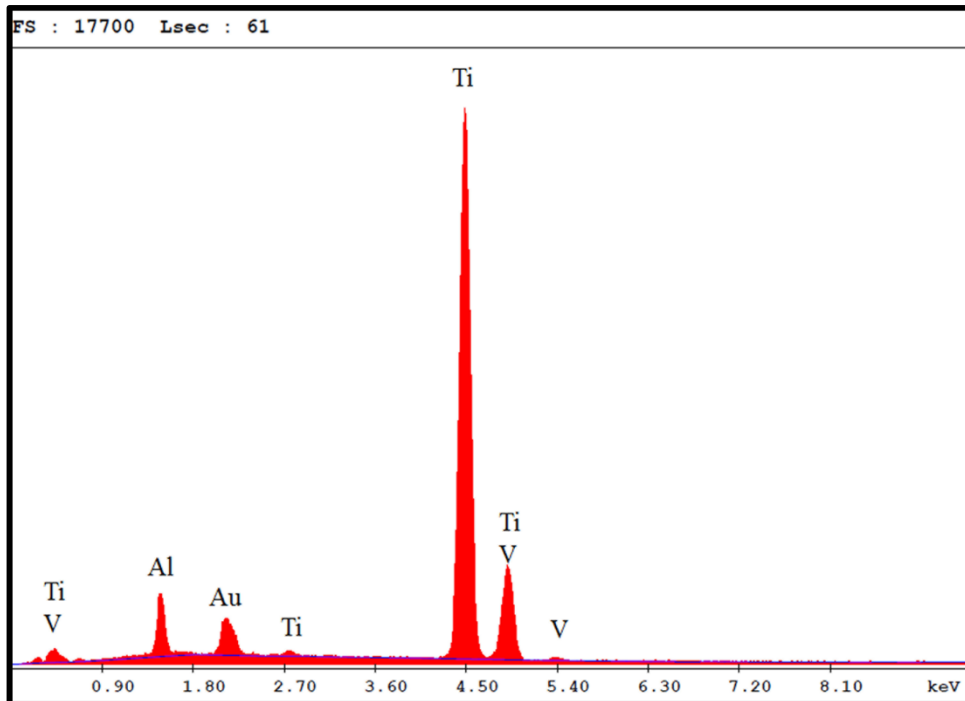
Compositions of each phase in the processed foams were determined by EDX attached to SEM. For the analysis only the  $K_{\alpha}$ -lines of the elements were used and aluminum rich phase was identified as  $\alpha$ -phase while the other vanadium rich phase was determined as BCC  $\beta$ -phase. The results of the analysis are given in Table 4.2 and Figure 4.5.

**Table 4.2** Weight percentages of the present phases.

<b>Element</b>	<b><math>\alpha</math> Phase (wt. %)</b>	<b><math>\beta</math> Phase (wt. %)</b>
<b>Ti</b>	90.67	87.96
<b>Al</b>	6.68	6.04
<b>V</b>	2.65	6.00



(a)



(b)

**Figure 4.5** EDX results of the phases (a)  $\alpha$  phase, (b)  $\beta$  phase.

## 4.3 Mechanical Behavior of Ti-6Al-4V Foams

### 4.3.1 Compressive Behavior

#### 4.3.1.1 Stress Strain Curves

Compressive stress-strain curves of Ti-6Al-4V foams produced via Mg space holder technique by sintering for 2h at 1200°C under high purity argon gas atmosphere are given in Figure 4.6. The foams manufactured in this study exhibited stress strain curves typical for elastic-plastic foams.

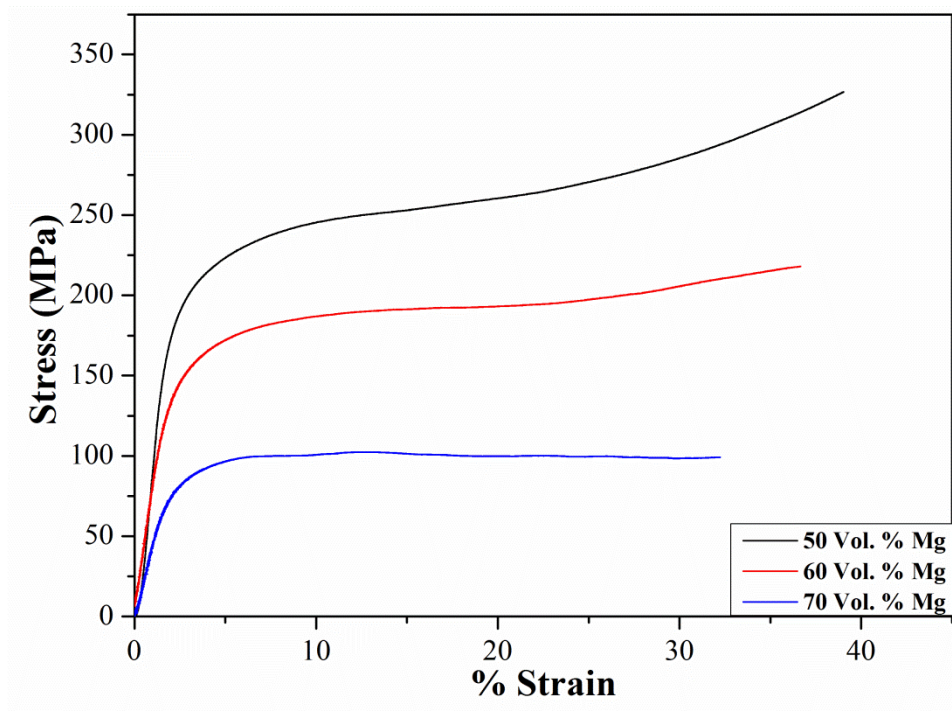


**Figure 4.6** Compressive stress strain curves of highly porous Ti-6Al-4V alloy sintered at 1200°C for 2h under high purity argon gas atmosphere.

The compressive stress strain curves of foams were divided into three distinct stages; a linear increase in stress and strain, a relatively long plateau region, where strain increases gradually with increasing stress and finally a region of rapid increase in stress [17].

In the first stage, the deformation of the foams occurred by elastic buckling, bending and extension of the cell walls. The deformation in this stage was macroscopically elastic. However, the complex alignment of cell walls and the presence of micropores created local stress concentrations on sinter necks causing localized plastic deformation below the yield strength of the foam. In the second stage, the stress acting on the cell walls induced macroscopic plastic deformation starting from weaker and thinner cell walls. Cell walls deform until the force acting on them reach a maximum value where failure and collapse of the cell walls occur (Figure 4.7).

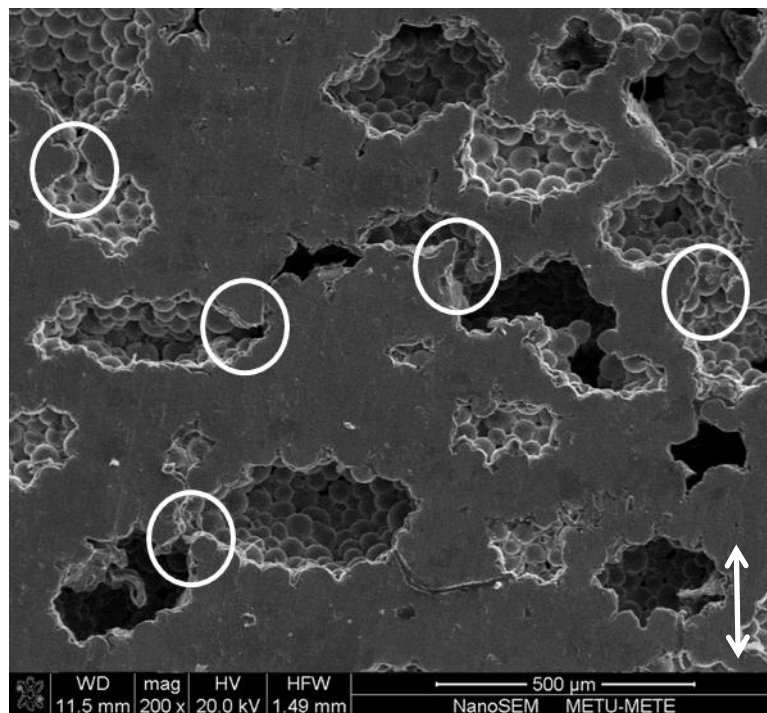


**Figure 4.7** Collapsed cell walls during compression.

Circles showing some of the failed cell walls and white arrow shows the direction of compression.

As a result of the collapse of cell walls, deformation lines perpendicular to the loading axis were observed on the specimens. The length and form of plateau region was significantly affected from the porosity content of the foam. Foams produced with 50 vol. % Mg addition showed shorter plateau and an upward slope in the plateau region. With increasing porosity, the slope of the plateau region

diminishes and its length increases. Foams manufactured with 70 vol. % Mg addition exhibited a horizontal wavy plateau region. The change of the mechanical response in the behavior of the plateau region was attributed to the geometry and amount of cell walls present in the foams. Foams with less porosity had thicker cell walls, which deform as a bulk rather than collapsing prematurely. This increases stiffness of the foam and results in short and sloping upward plateau primarily due to strain hardening effects. In the third stage, a rapid increase in stress was observed. This increase in stress is called as densification. The densification of the foams was caused by the increase in the effective net area due to collapse of the cell walls eventually. Foams manufactured with 70 vol. % Mg addition did not exhibit densification behavior due to excessive cell wall fractures before the collapse of the cell walls up to 30 % strain. Figure 4.8 shows the final shapes of the foams after compression. A summary of the mechanical properties of the foams are given in Table 4.3.

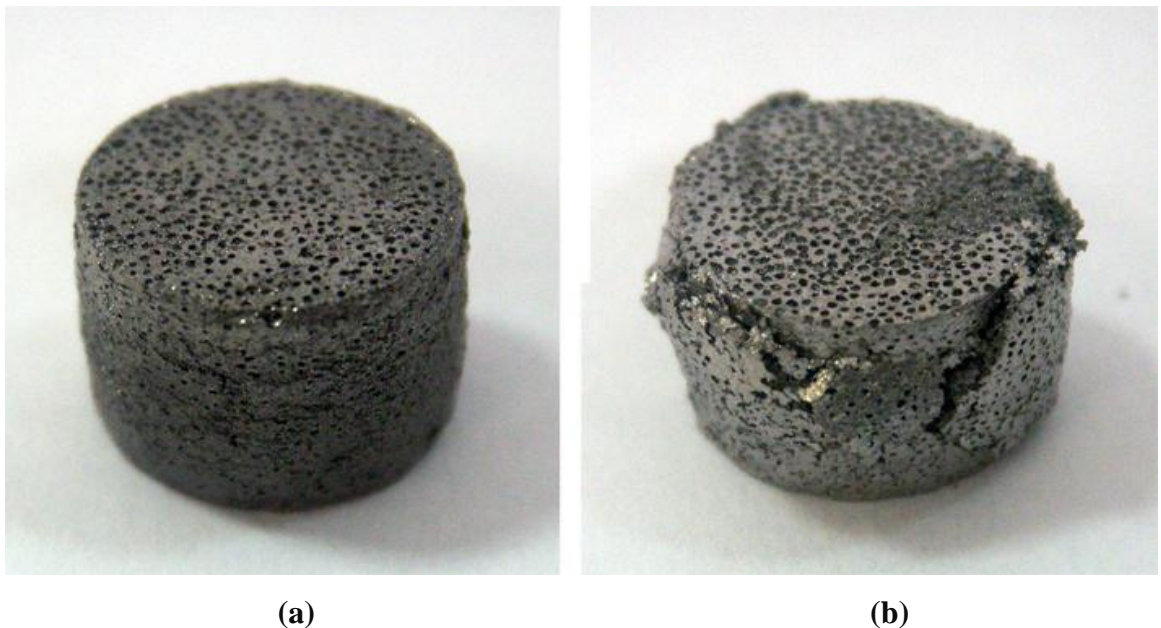


**Figure 4.8** Foams after compression tests (a) 50, 60 (b) 70 Vol. % Mg added foams.

**Table 4.3** Mechanical Properties of the Foams.

	<b>50Vol.% Mg</b>	<b>60Vol.% Mg</b>	<b>70Vol.% Mg</b>
$\sigma_y$ (MPa)	167 ± 18	125 ± 1.3	69 ± 3.4
$\sigma_{max}$ (MPa)	246± 23	185± 4.5	100 ± 6.6
<b>E (GPa)</b>	12.37 ± 1.46	7.99 ± 0.52	4.78 ± 0.67

#### 4.3.1.2 Cyclic Compressive Behavior

For the investigation of the plastic deformation of foam below the yield point, cyclic compression tests were conducted on foams produced using 60 vol. % Mg addition. Figure 4.9 shows the mechanical response of the foam below its yield point during loading and unloading. The y-axis of the figure was normalized with respect to the yield point of the foam for better interpretation of the diagram.

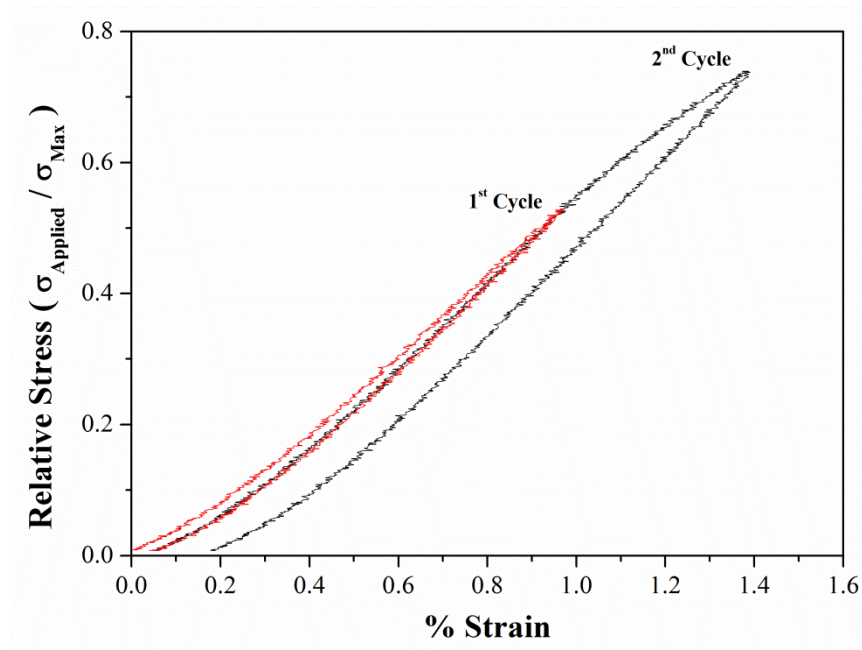


**Figure 4.9** Cyclic compression tests showing the residual strain below  $\sigma_{yield}$ .

Before the test parallelism of the foam surfaces was ensured with a precision of 10  $\mu\text{m}$  (0.11 % Strain). In the first cycle, where the foam was loaded up to  $0.55 \cdot \sigma_y$ , a contraction of 5  $\mu\text{m}$  (0.05 % strain) was remained after unloading the foam. In the second cycle the foam was loaded up to  $0.7 \cdot \sigma_y$  and the remaining contraction

increased up to 17  $\mu\text{m}$  (0.18 % strain). This was attributed to the plastic deformation of the sinter necks due to localized stress concentrations in the cell walls although the applied stress was below yield strength of the foams. In addition to residual strain analyses elastic modulus of the foam was also investigated. Figure 4.10 shows the change of relative elastic modulus with respect to % unrecovered strain applied on the test specimen.

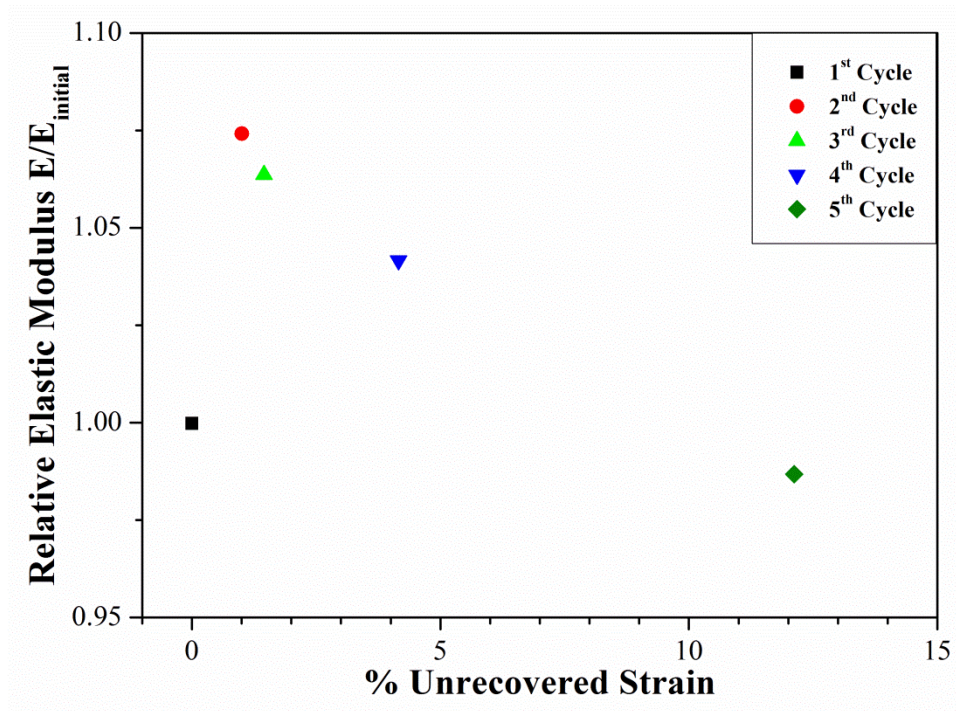


**Figure 4.10** Change of Relative elastic modulus of the foam.

Elastic modulus of the foam increased sharply at the first loading cycle while further straining the modulus dropped below the initially calculated value. The first increase was attributed to the formation of localized plastic deformation zones, which were creating micro plastic strain, on the favorably aligned sinternecks of the foam before yielding and the drop in the elastic modulus was thought to be a consequence of crack formation and individual failure of sinter necks.

### 4.3.1.3 Compressive Behavior - Porosity Relations

Mechanical properties of the foams were investigated with respect to the change in porosity percentage. Theoretical models use the density ratio of the foams and the bulk material properties for correlating the results. The models assume that the cell walls are made of 100 % bulk material. However, in the present study cell walls are made up of partially sintered powders so that relative density term should be calculated using cell wall density (3.71 g/cm<sup>3</sup>). The change of mechanical properties of the foams with relative density is given in Figure 4.11. The curves obeyed a power relationship in the form of

$$M = A \times (\text{relative density})^n \quad (4.2)$$

Where M is the related mechanical property of foam and A, n are constants

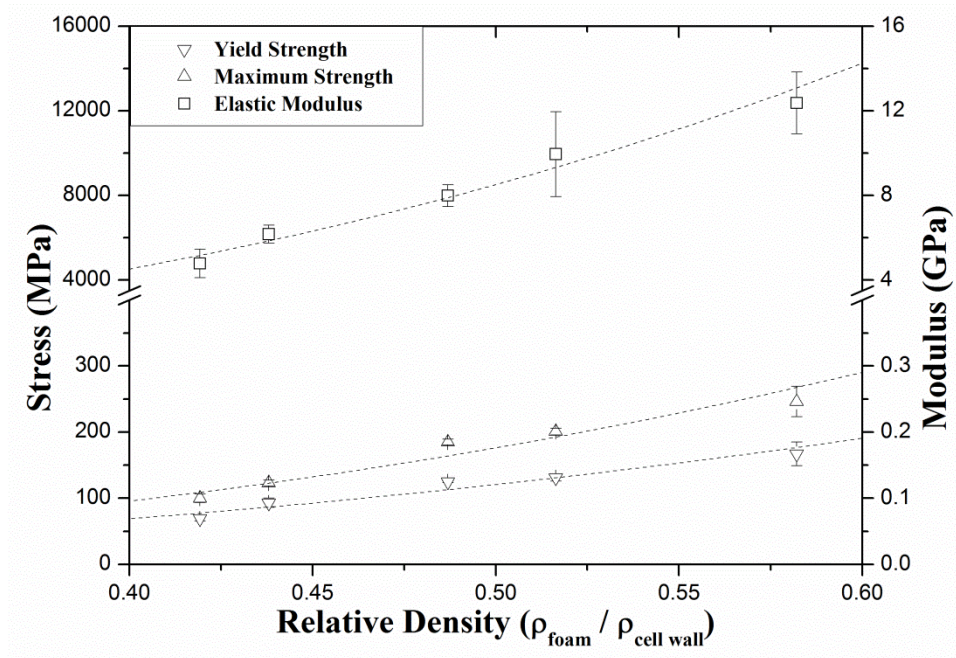


**Figure 4.11** Mechanical properties of the foams with respect to relative density.

Empirical relations obtained from the Figure 4.12 are summarized in Equations 4.3 - 4.5 as follows;

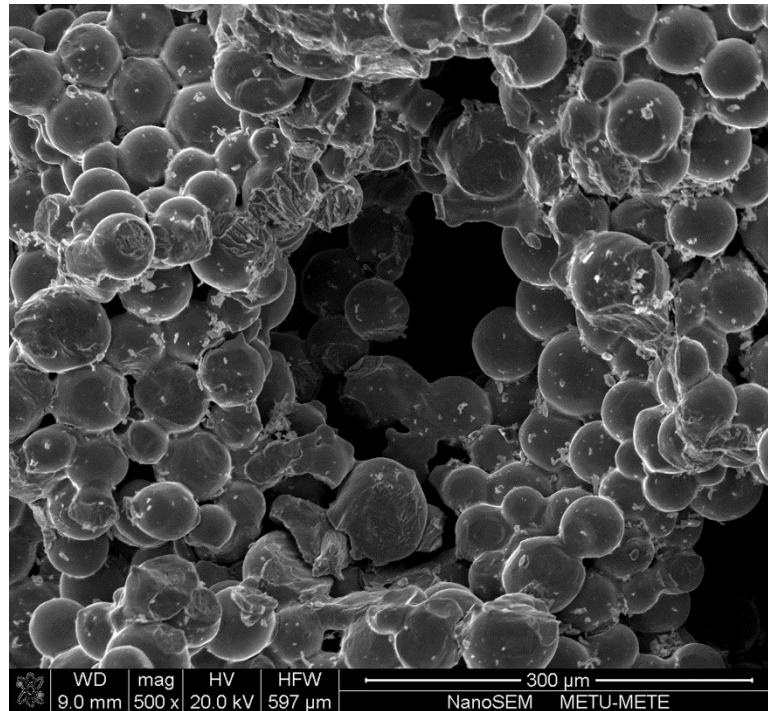
$$\sigma_{\text{yield}}(\text{MPa}) = 686.7 \times (\rho_{\text{foam}} / \rho_{\text{cell wall}})^{2.51} \quad R^2 = 0.9305 \quad (4.3)$$

$$\sigma_{\max}(\text{MPa}) = 1177.5 \times (\rho_{\text{foam}} / \rho_{\text{cell wall}})^{2.74} \quad R^2 = 0.9305 \quad (4.4)$$

$$E (\text{GPa}) = 60.4 \times (\rho_{\text{foam}} / \rho_{\text{cell wall}})^{2.82} \quad R^2 = 0.9709 \quad (4.5)$$

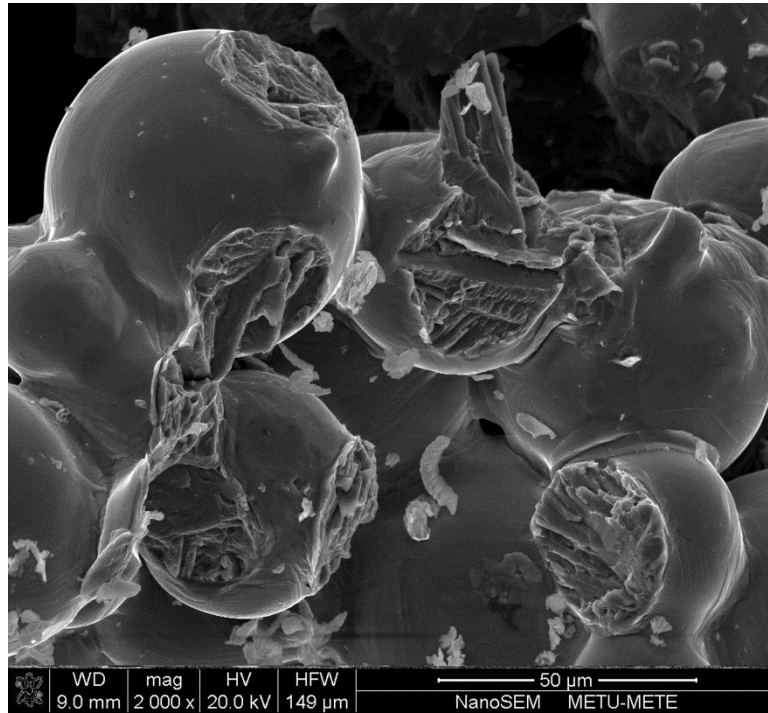
#### 4.3.1.4 Fracture Surfaces after Compression Tests

Fracture surface analyses were conducted on the samples to understand the nature of fracture. SEM micrographs revealed that the fracture of the cell walls originates from the failure of individual sinter necks. Fracture of the sinter necks between powder particles were mostly in ductile manner, containing dimples. However, some fracture surfaces contained transcrystalline tear ridge like appearance which were thought to originate from the  $\beta$  plates. Figure 4.12 shows some examples of fracture surfaces.

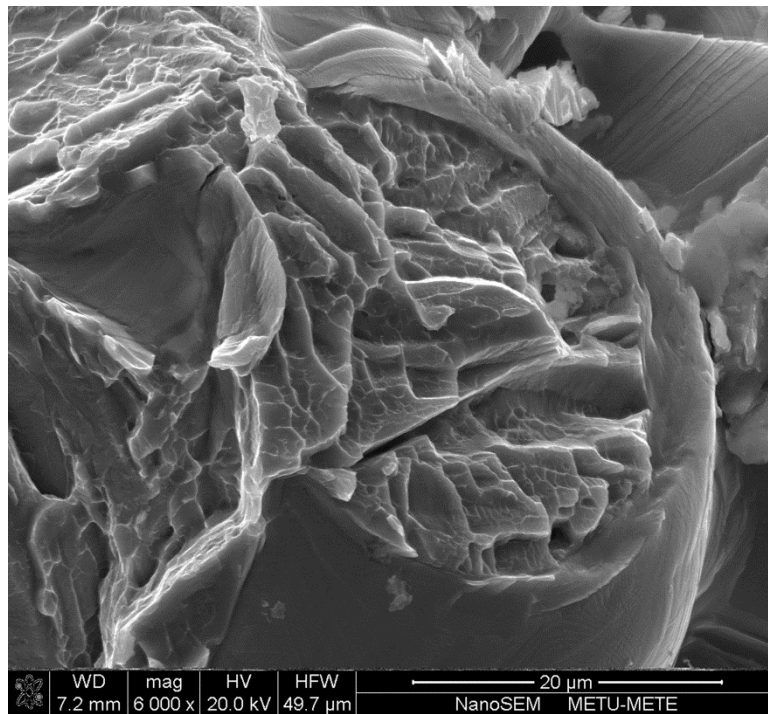


(a)

**Figure 4.12** SEM micrographs of tested foams (a) general view of fractured surfaces, (b) sinter necks containing tear ridge like appearance, (c) transcrystalline fracture feature with dimples on  $\alpha$  laths, (d) dimples.

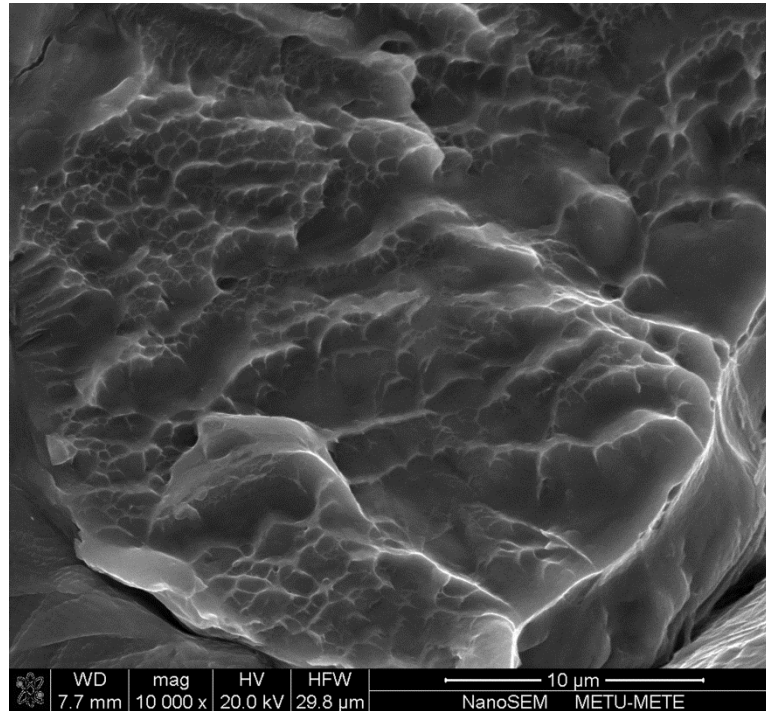


(b)



(c)

**Figure 4.12 (cont.)** SEM micrographs of tested foams (a) general view of fractured surfaces, (b) sinter necks containing tear ridge like appearance, (c) transcrystalline fracture feature with dimples on  $\alpha$  laths, (d) dimples.



(d)

**Figure 4.12 (cont.)** SEM micrographs of tested foams (a) general view of fractured surfaces, (b) sinter necks containing tear ridge like appearance, (c) transcrystalline fracture feature with dimples on  $\alpha$  laths, (d) dimples.

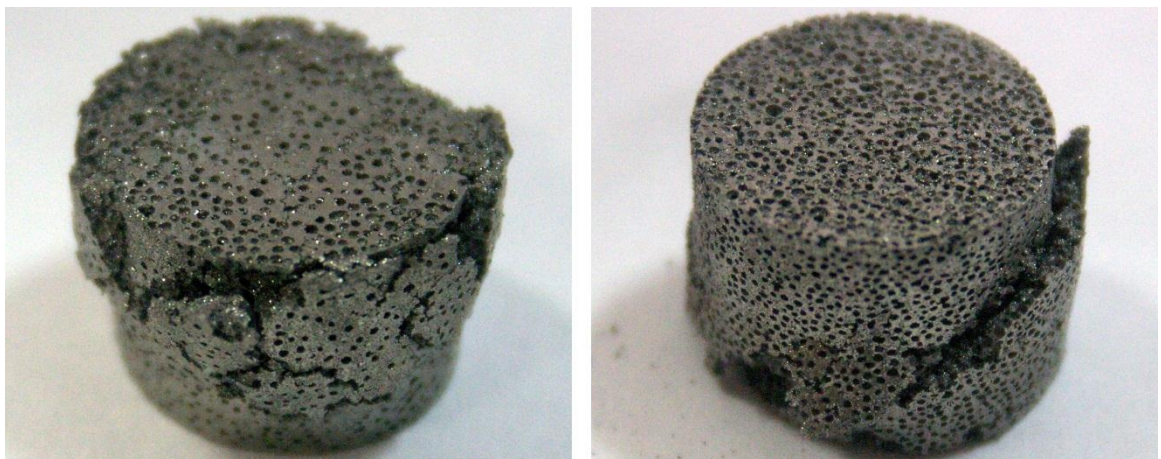
## 4.3.2 Fatigue Behavior

### 4.3.2.1 Contraction - # of Cycles Curves

Manufactured foams were tested under compressive-compressive fatigue at stress ratio  $R=0.1$ . Contraction - # of cycles curves drawn consisted of three definite regions. First two stages of the curves were similar for all foams; however, the final failure stage exhibited two different characteristics, as shown in Figure 4.13 and Figure 4.14.

In the first region at relatively low cycles, i.e. few hundred cycles, there was a rapid increase in contraction in first few hundred cycles. It was believed that this first region was due to localized plastic deformation on sinter necks. The second region was characterized by a long plateau on the contraction - # of cycles curves. In this

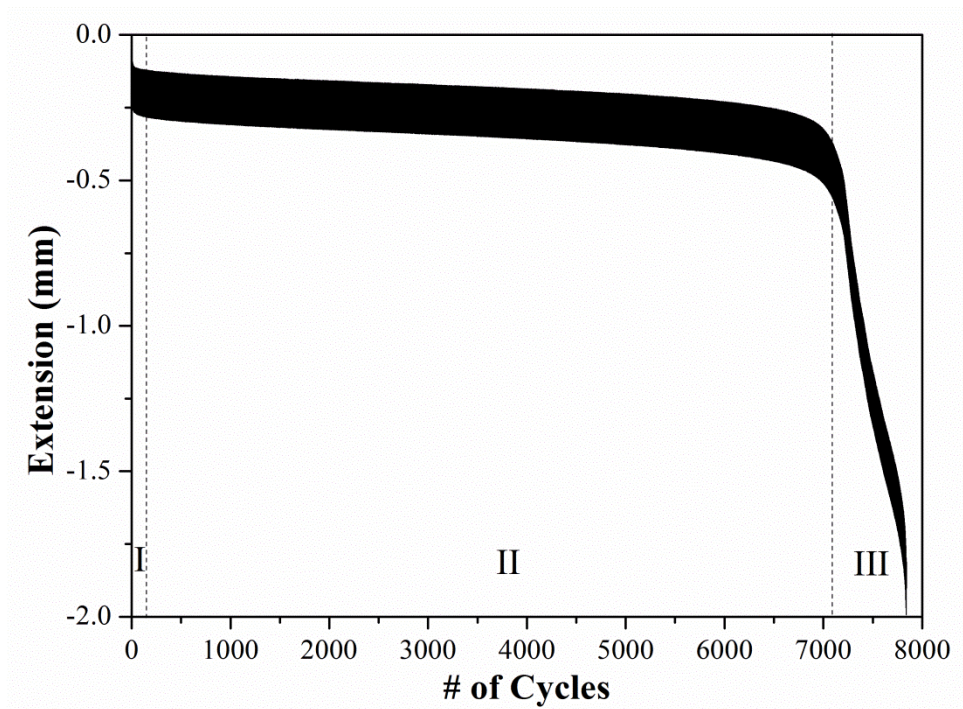
region contraction was observed to increase slowly throughout the cycles. The increase in the contraction was attributed to formation of microcracks on the sinter necks which were exposed to higher stress levels due to stress concentrations. The third region started with the formation of a knee on the curves. However, after knee formation, curves showed two different behaviors; a wavy increase in contraction (Figure 4.14.(a)) or a sharp increase in contraction (Figure 4.14.(b)). The wavy type of failure was observed in the foams manufactured with 50 and 60 vol. % Mg addition. The later was related to the foams processed with 70 vol. % Mg addition. In the literature the wavy type of failure was explained as introduction of deformation bands in to the structure and with each wave on the curve corresponds to deformation band crushing or collapsing. In addition, the sudden failure was explained as uniform accumulation of strain throughout the test specimen like the situation in homogeneous bulk materials [38]. Furthermore, these two different phenomena could be explained by correlating to compressive behavior of the foams. The foams which showed densification stage in compression test failed with wavy type of fatigue failure. It was attributed that thinnest cell walls of the foams with less porosity fails in sequence and contraction increases in a wavy nature, whereas cell walls of the foams with higher porosity buckles and bends uniformly and the failure occurs spontaneously leading to a single and rapid increase in contraction.



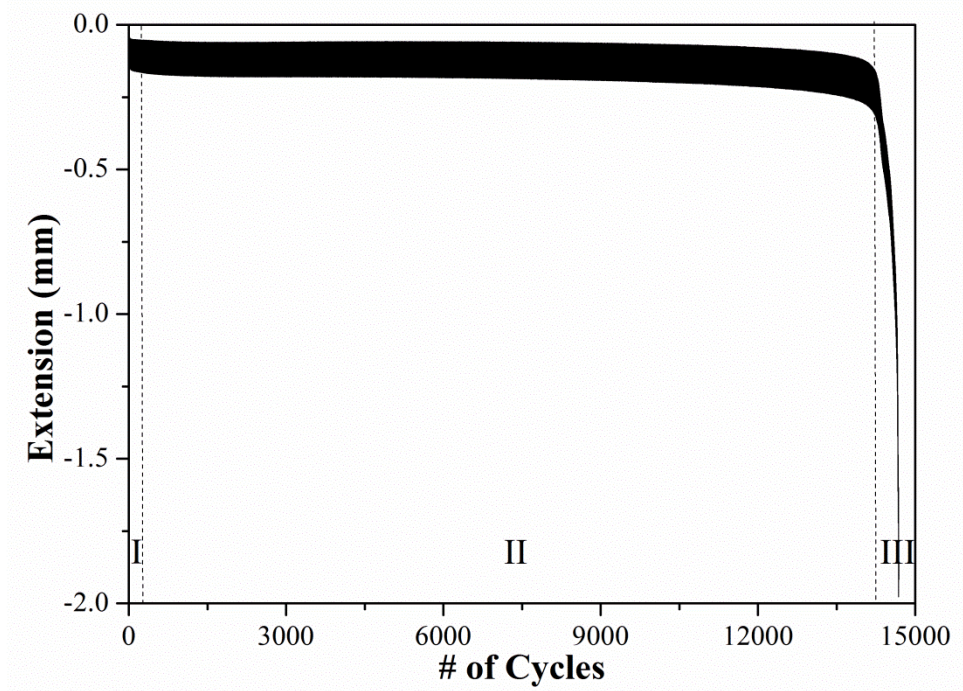
(a)

(b)

**Figure 4.13** Foams failed under cyclic loading. Samples (a) failed with wavy increase in contraction, (b) failed with rapid and sudden increase in contraction.



(a)



(b)

**Figure 4.14** Contraction - # of cycles curves of the processed foams (a) representative curve for foams exhibiting densification, (b) representative curve of the foams not exhibiting densification under quasi-static compression test.

### 4.3.2.2 S-N Curves

In order to draw the S-N curves compression-compression tests were conducted at different stress level with a constant R value. S-N curves for the foams tested were drawn as the maximum applied compressive stress versus the cycles to failure calculated from the knee point of the contraction curves. Figure 4.15 shows the S-N curve for the processed foams.

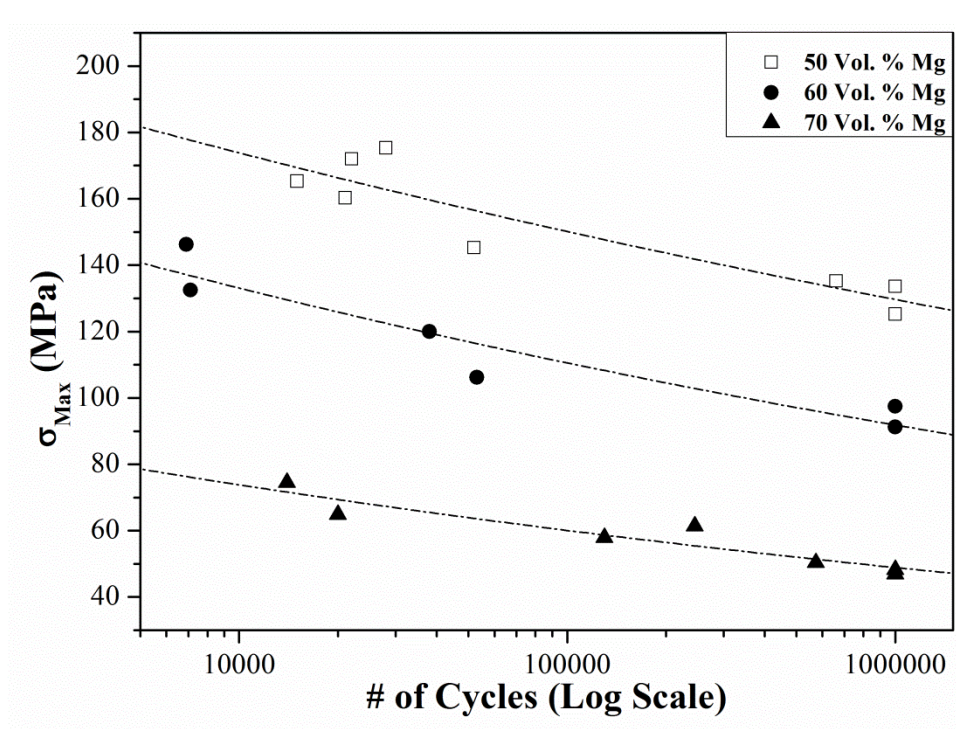
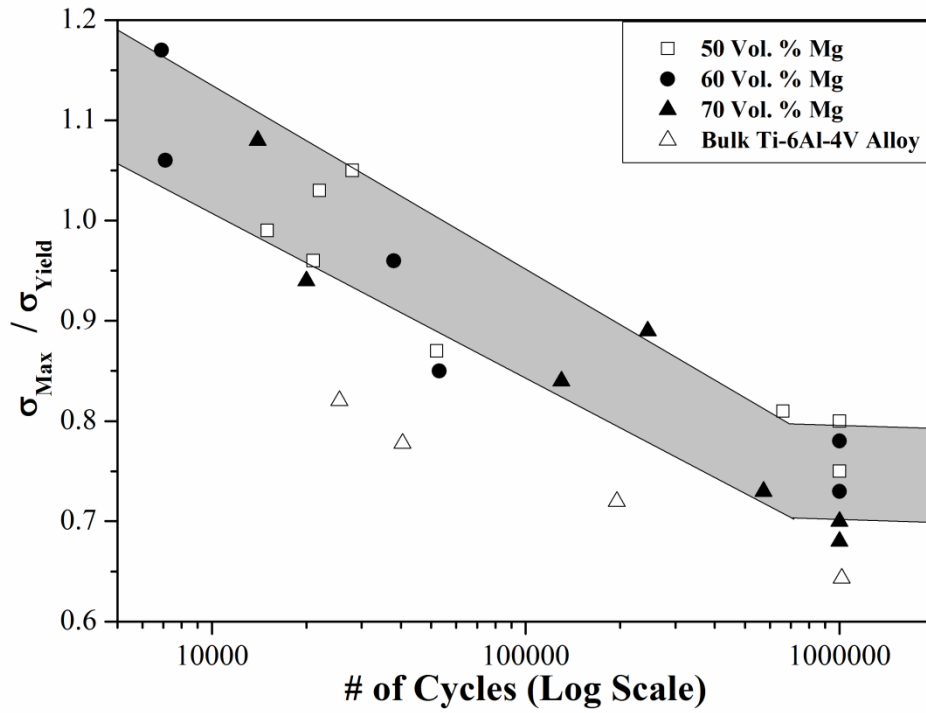


Figure 4.15 S-N curves of the processed foams.

Since fatigue behavior is known to be very sensitive to the strength of the alloy, to see how porosity content affects it, the maximum stress applied was normalized with respect to the foams average yield strength, Figure 4.16. In addition the results of Nalla et al. for bulk Ti-6Al-4V alloy with fully lamellar microstructure was shown in the same figure [39]. It was seen that after normalization all the results fit into a broad band as expected from the statistical nature of fatigue phenomena. This result yielded that fatigue behavior and endurance limit of the foams was independent of porosity content and the later was found to be in the range of  $(0.75 \pm 0.05) * \sigma_{max} / \sigma_{yield}$  for the present study.



**Figure 4.16** Normalized S-N curve of processed foams and bulk Ti-6Al-4V alloy [39].

### 4.3.2.3 Fracture Surfaces of Fatigue Tested Foams

Fracture surfaces were studied to investigate the differences in fracture mechanism with respect to the applied stress and porosity. However, the appearance of the fractured surfaces were similar to each other. It was also hard to identify the crack initiation and growth direction due to complexity in geometry of the foams. Some characteristic features of crack growth and catastrophic failure observed are shown in Figures 4.17 to 4.19. Figure 4.17 shows the striations due to fatigue crack growth (marked as A) and its orientation, and phase depended transgranular tear ridges (marked as B) formed during final failure. Furthermore, in many locations crack growth was observed in the form of striations and tire marks (Figure 4.18). In addition to fatigue crack growth, different types of fracture surfaces, which were also similar to those observed in quasi-static compression tests were observed (Figure 4.19).

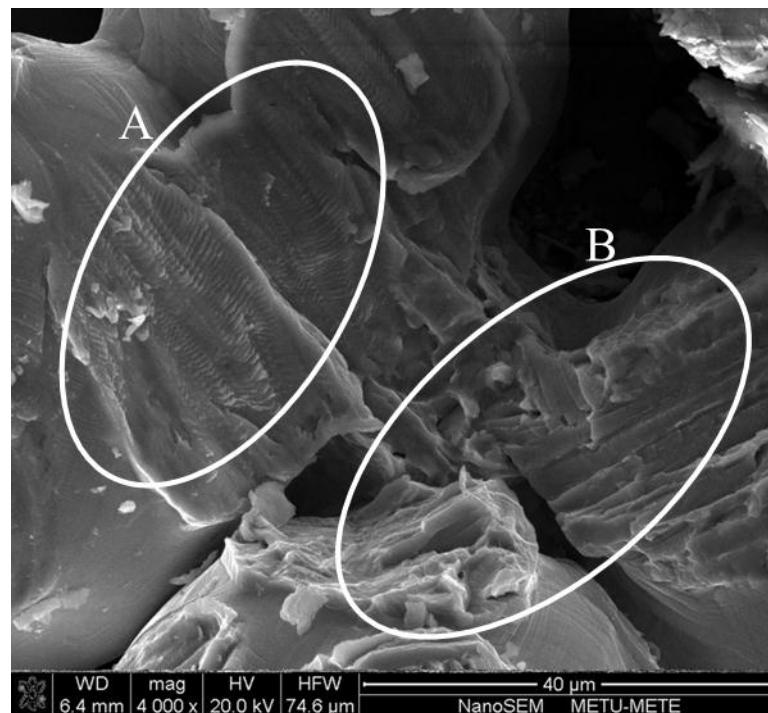
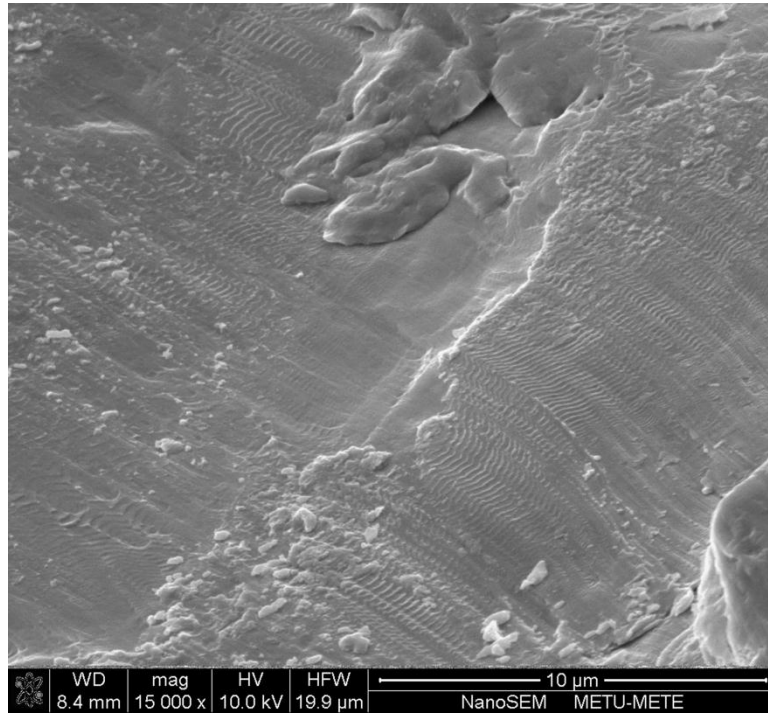
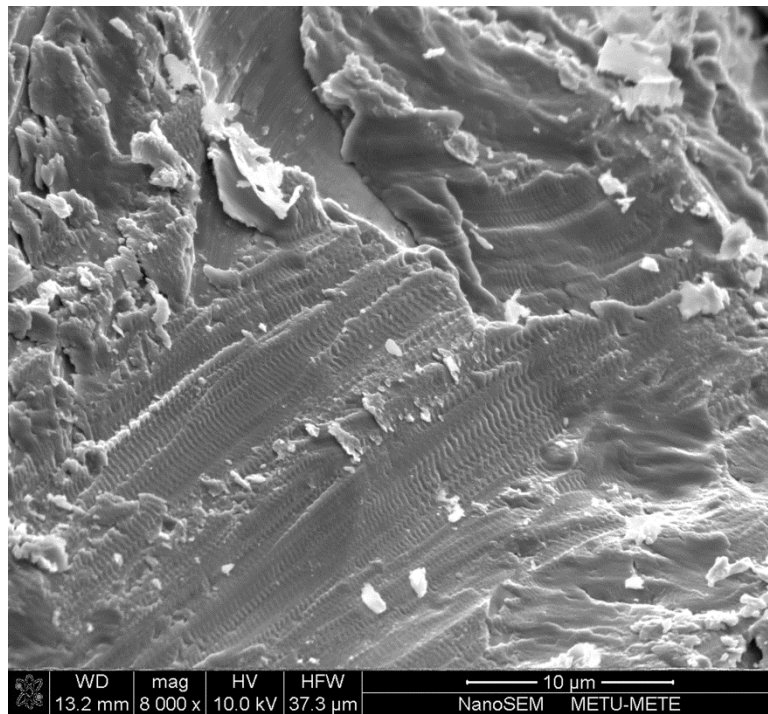


**Figure 4.17** Example of a crack growth and fracture.

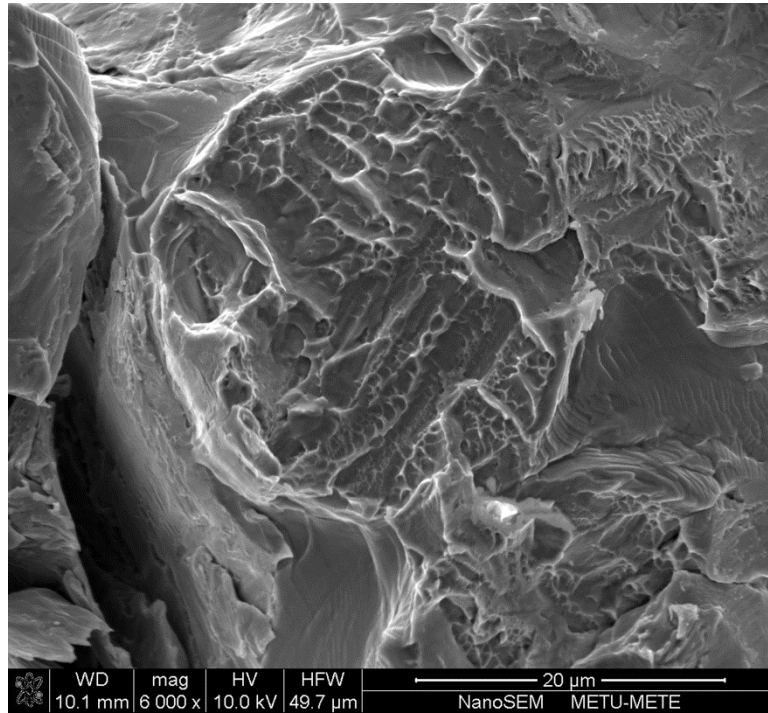


(a)

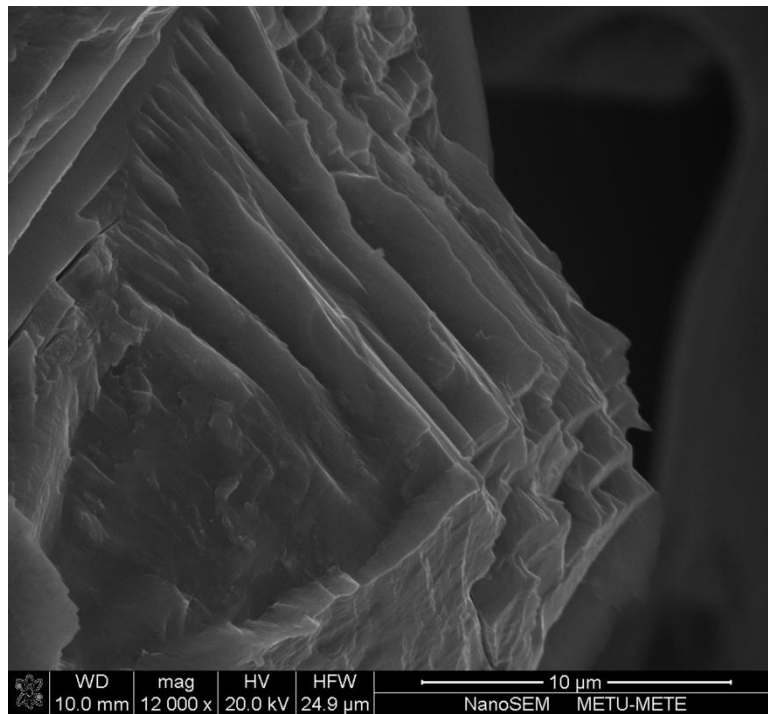


(b)

**Figure 4.18** Micrographs showing fatigue crack growth (a) striations, (b) tire marks.

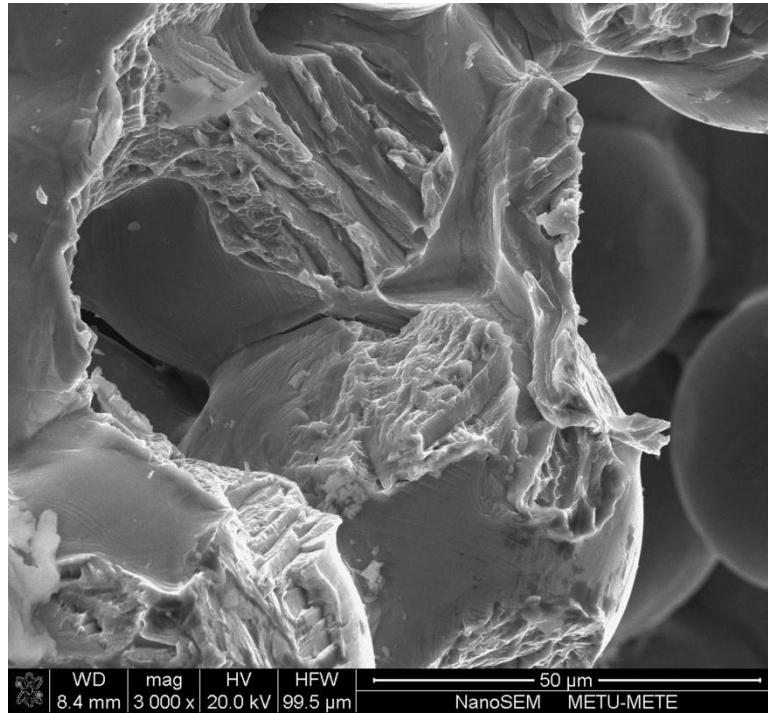


(a)



(b)

**Figure 4.19** Micrographs showing fast fracture surfaces (a) dimples, (b) tear ridges, (c) combination of tear ridges and dimples on possible  $\alpha$  laths.



(c)

**Figure 4.19 (cont.)** Micrographs showing fast fracture surfaces (a) dimples, (b) tear ridges, (c) combination of tear ridges and dimples on possible  $\alpha$  laths.

## CHAPTER 5

### CONCLUSION

1. Foams processed by utilizing magnesium as space holder yielded two types of pores, namely, macropores and micropores. Macropores, which were prior magnesium sites, were almost spherical in shape and interconnected with each other while the micropores, which were present due to insufficient sintering, were of irregular shape.
2. Cell walls were observed to have a density of  $3.71 \text{ g/cm}^3$  regardless of the porosity content.
3. There is a critical level of Mg around 57 vol. % below which the final porosity is lower than the added volume of the spacer due to collapse of some cell walls during heating.
4. Compressive stress - strain diagrams of the foams are composed of three stages, linear macroscopic elastic region, plateau region and densification region except the foams with 70 vol. % Mg addition which did not exhibit densification stage due to excess fracture of cell walls.
5. In the macroscopic elastic region it was found that there exists a micro-plastic strain due to stress concentrations on the sinter necks. Also, the loading moduli of the foams are affected from the presence of micro-plastic deformation.

6. The mechanical properties of the foams were found to obey a power law relationship in the form of  $M = A \times (\text{relative density})^n$ , where  $M$  is the mechanical property of foam and  $A$  and  $n$  are constants.
7. Under cyclic loading conditions, all of the foams deformed in three steps; a rapid increase in contraction, a constant accumulated contraction regime and rapid increase in contraction leading to failure.
8. Foams exhibited two types of failure characteristics under cyclic loading. Foams with lower porosities exhibited a wavy failure which indicates presence of a crush band. On the other hand, foams with higher porosity content failed suddenly with a single collapse.
9. The fatigue limits of the foams are widely spread but when maximum applied stresses are normalized with respect to the yield strength of the foams, fatigue behavior of the foams are set on a band. In addition, it is found that processed foams are fatigue immune with a practical limit of  $10^6$  cycles under a maximum applied stress of  $(0.75 \pm 0.05) \cdot \sigma_{\max} / \sigma_{\text{yield}}$ .

## REFERENCES

- [1] D.M. Brunette, P. Tengvall, M. Textor, P. Thomsen, Titanium in Medicine: Material Science, Surface Science, Engineering, Biological Responses and Medical Applications, Springer, Verlag Berlin Heidelberg, 2001.
- [2] G. Lütjering, J.C. Williams, Titanium, Springer, Verlag Berlin Heidelberg, 2003.
- [3] D. Eylon, S.R. Seagle, Titanium '99: Science and Technology, CRISM "PROMETEY". (1999) 37.
- [4] G. Lütjering, Influence of processing on microstructure and mechanical properties of ( $\alpha+\beta$ ) titanium alloys, Materials Science and Engineering: A. 243 (1998) 32-45.
- [5] C. Leyens, M. Peters, Titanium and Titanium Alloys: Fundamentals and Applications, Wiley-VCH, Weinheim Germany, 2003.
- [6] B.D. Ratner, A.S. Hoffman, F.J. Schoen, J.E. Lemons, Biomaterials Science: An Introduction to Materials in Medicine, Elsevier, Great Britain, 1996.
- [7] Y. Oshida, Bioscience and Bioengineering of Titanium Materials, Elsevier, Great Britain, 2007.
- [8] D.R. Sumner, T.M. Turner, R. Igloria, R.M. Urban, J.O. Galante, Functional adaptation and ingrowth of bone vary as a function of hip implant stiffness, J. Biomech. 31 (1998) 909-917.
- [9] J. Black, G.W. Hastings, Handbook of Biomaterials Properties, Chapman and Hall, London UK, 1998.
- [10] P. Branemark, Osseointegration and its experimental background, J. Prosthet. Dent. 50 (1983) 399-410.

- [11] M. Jasty, C. Bragdon, S. Schutzer, H. Rubash, T. Haire, W. Harris, Bone ingrowth into porous coated canine total hip replacements. Quantification by backscattered scanning electron microscopy and image analysis, *Scanning Microsc.* 3 (1989) 1051.
- [12] H. Kienapfel, C. Sprey, A. Wilke, P. Griss, Implant fixation by bone ingrowth, *J. Arthroplasty.* 14 (1999) 355-368.
- [13] Z. Esen, E. Tarhan Bor, Ş. Bor, Characterization of loose powder sintered porous titanium and Ti6Al4V alloy, *Turkish Journal of Engineering and Environmental Sciences.* 33 (2009) 207-219.
- [14] N.W. Hrabe, P. Heintl, B. Flinn, C. Körner, R.K. Bordia, Compression-compression fatigue of selective electron beam melted cellular titanium (Ti-6Al-4V), *J. Biomed. Mater. Res. Part B Appl. Biomater.* 99 B (2011) 313-320.
- [15] D.J. Jorgensen, D.C. Dunand, Ti-6Al-4V with micro- and macropores produced by powder sintering and electrochemical dissolution of steel wires, *Materials Science and Engineering: A.* 527 (2010) 849-853.
- [16] M. Niinomi, Mechanical biocompatibilities of titanium alloys for biomedical applications, *Journal of the Mechanical Behavior of Biomedical Materials.* 1 (2008) 30-42.
- [17] L.J. Gibson, M.F. Ashby, *Cellular Solids: Structure and Properties*, Cambridge University Press, Great Britain, 1999.
- [18] J. Banhart, Manufacture, characterization and application of cellular metals and metal foams, *Progress in Materials Science.* 46 (2001) 559-632.
- [19] D.C. Dunand, Processing of Titanium Foams, *Advanced Engineering Materials.* 6 (2004) 369-376.
- [20] S. Oppenheimer, D.C. Dunand, Solid-state foaming of Ti-6Al-4V by creep or superplastic expansion of argon-filled pores, *Acta Materialia.* 58 (2010) 4387-4397.

- [21] M.F. Ashby, A.G. Evans, N.A. Fleck, L.J. Gibson, J.W. Hutchinson, H.N.G. Wadley, *Metal Foams: A Design Guide*, Butterworth-Heinemann, United States of America, 2000.
- [22] Z. Esen, Ş. Bor, Characterization of Ti-6Al-4V alloy foams synthesized by space holder technique, *Materials Science and Engineering A*. 528 (2011) 3200-3209.
- [23] G. Ryan, A. Pandit, D.P. Apatsidis, Fabrication methods of porous metals for use in orthopaedic applications, *Biomaterials*. 27 (2006) 2651-2670.
- [24] M. Sharma, G.K. Gupta, O.P. Modi, B.K. Prasad, A.K. Gupta, Titanium foam through powder metallurgy route using acicular urea particles as space holder, *Mater Lett*. 65 (2011) 3199-3201.
- [25] A. Mansourighasri, N. Muhamad, A.B. Sulong, Processing titanium foams using tapioca starch as a space holder, *J. Mater. Process. Technol*. 212 (2012) 83-89.
- [26] A. Bansiddhi, D.C. Dunand, Shape-memory NiTi foams produced by replication of NaCl space-holders, *Acta Biomaterialia*. 4 (2008) 1996-2007.
- [27] B. Arpak, K. Araz, İ. Nakaş, Ş. Bor, The mechanical characterization and in-vivo evaluation of porous TiNi as graft material, *Funct. Mater. Lett.* (2012).
- [28] R.W. Cahn, P. Haasen, *Physical Metallurgy*, Elsevier, Netherlands, 1996.
- [29] L.C. De Jonghe, M.N. Rahaman, Chapter 4 - 4.1 Sintering of Ceramics, *Handbook of Advanced Ceramics*, Academic Press, Oxford, 2003, pp. 187-264.
- [30] L.J. Gibson, M.F. Ashby, The Mechanics of Three-Dimensional Cellular Materials, *Proceedings of the Royal Society of London. A. Mathematical and Physical Sciences*. 382 (1982) 43-59.
- [31] L.J. Gibson, Biomechanics of cellular solids, *J. Biomech*. 38 (2005) 377-399.

[32] S.R. Lampman, ASM Handbook: Volume 19: Fatigue and Fracture, ASM International, United States of America, 1997.

[33] A.H. Cottrell, D. Hull, Proc. R. Soc. (London) A. A242 (1957) 211.

[34] P. Neumann, Acta Metall. 17 (1969) 1219.

[35] W.F. Hosford, Mechanical Behavior of Materials, Cambridge University Press, United States of America, 2010.

[36] J. McCall, P.M. French, Metallography in Failure Analysis, Plenum Press, United States of America, 1978.

[37] Y. Sugimura, A. Rabiei, A.G. Evans, A.M. Harte, N.A. Fleck, Compression fatigue of a cellular Al alloy, Materials Science and Engineering: A. 269 (1999) 38-48.

[38] A. Harte, N.A. Fleck, M.F. Ashby, Fatigue failure of an open cell and a closed cell aluminum alloy foam, Acta Materialia. 47 (1999) 2511-2524.

[39] R.K. Nalla, B.L. Boyce, J.P. Campbell, J.O. Peters, R.O. Ritchie, Influence of microstructure on high-cycle fatigue of Ti-6Al-4V: Bimodal vs. lamellar structures, Metal Mat Trans A Phys Metal Mat Sci. 33 (2002) 899-918.